This is a non-peer-reviewed preprint submitted to EarthArXiv.

If you have any questions or suggestions, please contact the corresponding author by email at biancavale01@gmail.com.

All data used in the preparation of this manuscript are available at:

https://doi.org/10.5281/zenodo.23574830

This version was finalized for submission to EarthArXiv on October 22, 2026.

Bianca Soares do Vale

https://orcid.org/0000-0001-8770-5684

Elder Yokoyama

https://orcid.org/0000-0003-4246-6282

Uidemar Morais Barral

https://orcid.org/0000-0002-6876-2883

Janine Araujo do Carmo

https://orcid.org/0000-0003-3683-3648

Arthur Siqueira de Macedo

https://orcid.org/0009-0006-5106-4356

Adriana Maria Coimbra Horbe

https://orcid.org/0000-0001-6915-6685

Alexandre Silva Santos

https://orcid.org/0000-0001-9929-0201

Sebastião William da Silva

https://orcid.org/0000-0003-4483-9687

Pedogenic magnetic enhancement in a Latossolo Vermelho (Oxisol) formed on slate in the Brazilian Cerrado: an integrated record of repeated wetting–drying cycles

Bianca Soares do Vale*[a], Elder Yokoyama*[a], Uidemar Morais Barral[a], Janine Araujo do Carmo[b], Arthur Siqueira de Macêdo[b], Adriana Maria Coimbra Horbe[a], Alexandre Silva Santos[c], Sebastião William da Silva[c]

[a] University of Brasília, Institute of Geosciences, Brasília, DF, Brazil.

[b] University of São Paulo, Institute of Astronomy, Geophysics and Atmospheric Sciences, São Paulo, SP, Brazil.

[c] University of Brasília, Institute of Physics, Brasília, DF, Brazil.

* Corresponding authors. E-mail addresses: biancavale01@gmail.com (B. Vale), eyokoyama@unb.br (E. Yokoyama)

Abstract

Seasonal wetting–drying cycles in tropical soils can drive redox reactions that control the formation and transformation of ferrimagnetic iron oxides. In the profile-scale case study, we investigated a well-drained, clayey *Latossolo Vermelho* (Oxisol/ Ferralsol) developed on weakly magnetic slate in the Brazilian Cerrado. The profile was sampled to 190 cm depth in the dry season (July 2023) and at the end of the wet season (April 2024). Magnetic susceptibility, thermomagnetic curves, hysteresis loops, first-order reversal curves, isothermal and anhysteretic remanent magnetization, and coercivity spectrum unmixing were combined with soil properties, X-ray diffraction, and Raman and ATR-FTIR spectroscopy. Low-field susceptibility on the upper horizons (up to ~233 × 10^{-8} m^3 kg^{-1}) was more than 30 times higher than that of the parent slate (~6 × 10^{-8} m^3 kg^{-1}), and the soil is dominated by low-coercivity ferrimagnets, whereas the slate is dominated by high-coercivity hematite. High frequency-dependent susceptibility (~12%) and median ARM acquisition fields of ~12–13 mT indicate a fine-grained (superparamagnetic to single-domain) magnetite–maghemite assemblage, probably spanning a range of oxidation states, coexisting with hematite. The magnetic enhancement is therefore predominantly pedogenic. Despite contrasting hydrological conditions, seasonal differences were subtle, indicating that the magnetic signature reflects an integrated memory of repeated wetting–drying cycles rather than a rapidly reversible response to a single season. The mineral assemblage and pedoclimatic setting

are consistent with a long-term mechanism, inferred rather than directly observed, involving magnetite neoformation in transiently anoxic microsites, possibly through microbial Fe (III) reduction, followed by partial oxidation to maghemite.

Keywords: Environmental magnetism; Pedogenic magnetite; Maghemite; Redox cycling; Ferralsol; Oxisol; Cerrado

1. Introduction

Tropical soils play essential functions in regulating natural resources and maintaining biodiversity, covering more than a third of the Earth's terrestrial surface (Eswaran et al., 1992). These soils harbor a complex assemblage of pedogenic iron oxides, which are fundamental minerals for soil system functioning (Churchman and Lowe, 2012). Among tropical soil classes, *Latossolos* (SiBCS, 2025), corresponding to Ferralsols (IUSS Working Group WRB, 2022) and Oxisols (Soil Survey Staff, 2022), can exhibit a high proportion of iron oxides in their mineral composition resulting from residual accumulation associated with ferrallitization, a process driven by intense desilication activity (Kämpf and Curi, 2000; Ker et al., 2012).

The occurrence and intrinsic characteristics of these iron oxide minerals reflect the climatic and pedogenic conditions under which they were formed and transformed. Because they act as sensitive indicators of pedoenvironmental conditions and due to their magnetic properties, iron oxides minerals are the core focus of numerous environmental and soil magnetism studies (Torrent et al., 1983; Schwertmann, 1985; Thompson and Oldfield, 1986; Maher and Taylor,1988; Maher,1998; Evans and Heller, 2003; Liu et al., 2012; Jordanova, 2016; Maxbauer et al., 2016a; Barbosa et al., 2021; Gao et al., 2022; Reethu et al., 2023; Zhang et al., 2025; Lepre, 2026).

In soils, iron oxide minerals can exhibit diverse compositions and grain sizes. In cyclic soil activity, fine-grained pedogenic minerals form *in situ* through authigenic processes, mediated by inorganic chemical reactions and potential biological activities (Cornell and Schwertmann, 2003; Evans and Heller, 2003; Maxbauer et al., 2016a). When formed through pedogenesis, ferrimagnetic particles such as magnetite and maghemite differentiate and enhance the magnetic signature of upper soil horizons (Maher, 1998).

Several studies linked the degree of magnetic enhancement in soil surfaces to climatic variability (Tite and Linington, 1975; Maher and Thompson, 1992, 1995; Maher et al., 1994; Han et al., 1996; Maher, 1998; Balsam et al., 2011; Hu et al., 2015; Lepre, 2023). Despite these efforts, no single mechanism describes how different soil classes under varying climatic regimes are magnetically enhanced, given the complexity, diversity, and potential interactions among the involved processes (Evans and Heller, 2003; Jordanova, 2016; Maxbauer et al., 2016a). Furthermore, differing perceptions persist regarding the dominant influence of temperature versus moisture on the pedogenic formation of ferrimagnetic particles (Lepre, 2023). The debate also

extends to the specific magnetic mineral formed via pedogenesis, raising questions about whether magnetite or maghemite is the dominant phase under different environmental conditions (Maher, 1998; Barrón and Torrent, 2002; Torrent et al., 2006; Ahmed and Maher, 2018).

The mechanism explaining the magnetic enhancement, where maghemite is the primary ferrimagnetic phase (Barrón and Torrent, 2002; Torrent et al., 2006), proposes that, under warm, predominantly aerobic conditions and in the presence of ligands such as phosphate, ferrihydrite transforms via the pathway: ferrihydrite → SP maghemite → SD maghemite → hematite. This enhancement pathway is commonly reported for red soils with high hematite proportions (Hu et al., 2015; Long et al., 2015; Gao et al., 2018), including Brazilian *Latossolos* (Camêlo et al., 2017; Ramos et al., 2017; Poggere et al., 2018). However, the ferrihydrite aging model lacks a pathway for the pedogenic formation of magnetite in soils (Maxbauer et al., 2016a), whose origin is usually attributed to lithogenic inheritance (Torrent et al., 2006). Therefore, this pathway alone cannot readily explain the presence of magnetite on the upper horizons of soils developed from rocks with weak magnetic signatures under the tropical conditions of the Brazilian Cerrado, which differ from Mediterranean environments (Viana et al., 2016; Preetz et al., 2017).

In this context, one pathway for pedogenic magnetite formation occurs in well-drained soils subject to seasonal oxidation, under pH conditions ranging from 5.5 to 7.0 (slightly acidic to near-neutral) (Taylor et al., 1987; Maher et al., 2003). Dissimilatory Fe (III) - reducing bacteria can mediate this process. For magnetite to precipitate extracellularly, Fe^{2+} must be available in the soil solution, along with organic matter and anoxic microsites (Lovley et al., 1987; Maher, 1998; Hanesch and Petersen, 1999).

In the Brazilian Cerrado, the tropical conditions promote alternating soil wetting and drying cycles, favoring anaerobic zones within certain pores. Thus, under adequate biogeochemical conditions, the recurrence of these seasonal events can direct the degree of magnetic enhancement in upper soil horizons (Maher, 1998; Maher et al., 2003; Orgeira et al., 2011; Preetz et al., 2017; Ahmed and Maher, 2018).

Here, we characterize the magnetic mineralogy of a *Latossolo Vermelho* (Oxisol) developed from weakly magnetic slate, sampled in the dry season and at the end of the wet season in the Brazilian Cerrado. We address three questions: (i) is the magnetic enhancement of the upper

horizons inherited from the parent rock or produced by pedogenesis? (ii) Which ferrimagnetic phases, grain sizes, and domain states carry this enhancement? And (iii) do the magnetic properties record measurable seasonal differences that can be linked to wetting–drying redox cycles? We hypothesize that the enhancement is pedogenic. If the magnetic assemblage reflects the cumulative effects of multiple wetting–drying cycles, the seasonal differences between a single dry and wet period are expected to be minor compared to the contrast between the soil and its parent rock. Finally, we assess whether the observed assemblage aligns with magnetite neoformation in transiently anoxic microsites, followed by partial oxidation to maghemite, a mechanism that is proposed here rather than directly tested.

2. Materials and methods

2.1 Study area and sampling

The study was conducted at Fazenda Água Limpa (FAL) (15°56' 14" S, 47°46' 08" W) at an altitude of ~1,100 m in the Federal District, Brazil (Fig. 1a, b). Encompassing approximately 4,340 hectares, FAL is an Experimental Farm and Ecological Station owned by the University of Brasília (UnB). The lithology is dominated by clay-rich metasedimentary rocks of the Paranoá Group (Campos et al., 2013). The regional climate is tropical with dry winters (Aw/Cwa in the Köppen classification; Alvares et al., 2013), with a mean annual temperature of ~22 °C and two distinct seasons. The dry season extends from May to September, with an average relative humidity of 47%, dropping to 15% during the driest period. The rainy season extends from October to April, with a mean annual precipitation of ~1,600 mm (Golfari, 1978; Souza and Oliveira Júnior, 2026).

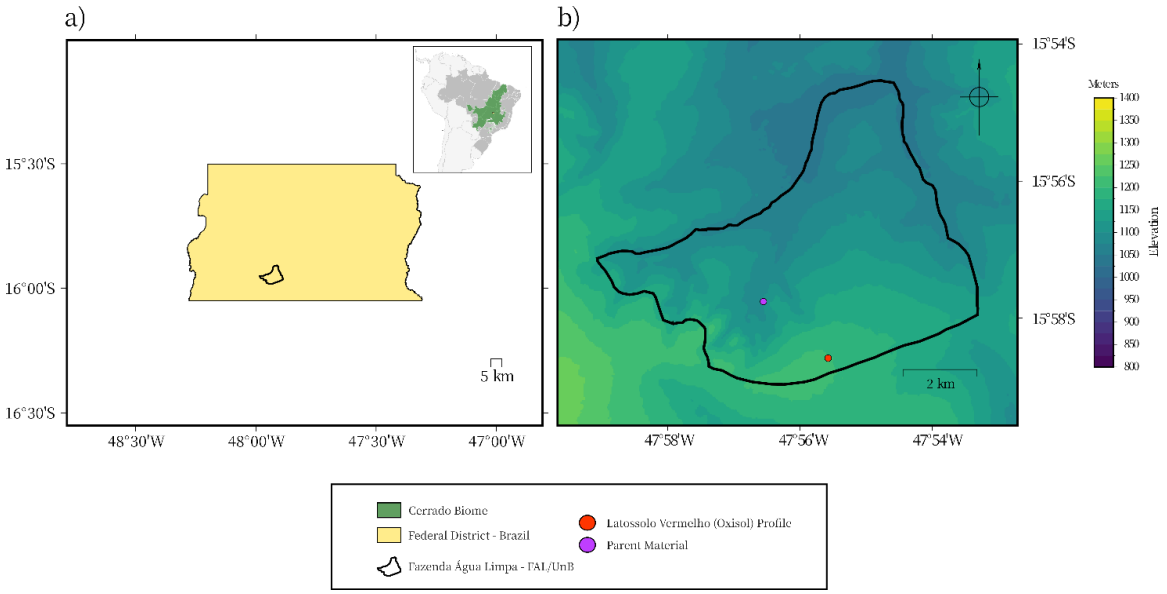


Figure 1. Location map of the study area. Coordinate reference system: WGS 84.

Weathering of the metasedimentary rocks of the Paranoá Group formed a clayey *Latossolo Vermelho Ácrico típico* (LVw) profile in the SiBCS classification (Acric Ferralsol in WRB; Acrustox in Soil Taxonomy) at 1,217 m (Fig. 1b; SFig. 1; Table S1), characterized by high drainage capacity. The area features a flat relief and is predominantly covered by native Cerrado vegetation (Barbosa et al., 2009; Campos et al., 2010).

To compare the magnetic properties of the studied soil profile under contrasting hydrological conditions, samples were collected in two distinct periods. The first collection took place on July 26, 2023, during the drying season (DS). The second sample collection occurred on April 30, 2024, at the end of the wetting season (WS), after the soil had received ~1,305 mm of precipitation since October 2023.

Wetting-season sampling took place six days after a precipitation event to allow soil moisture to reach field capacity. Soil sampling under saturated conditions would not accurately represent the *Latossolo Vermelho* (Oxisol) class, which has high drainage capacity and an absence of redoximorphic features. Meteorological data were obtained from the Climatological Station of Fazenda Água Limpa (FAL/UnB), which has over 20 years of meteorological parameter records available at: FAL - Fazenda Água Limpa - Laboratório de Agroclimatologia.

2.2 Soil properties

In the LVw profile, sampling in the drying and wetting seasons, approximately 400 g of undisturbed samples from each horizon (A, AB, BA and Bw) were collected and packed in plastic bags. These samples were sent to the Laboratory of Geochemistry (LAGEQ) at the Institute of Geosciences of the University of Brasília to determine the gravimetric moisture content of the horizons.

Following Teixeira et al. (2017), about 3 g of each sample were placed in triplicate into pre-weighed porcelain crucibles. The samples were oven-dried at 105°C for 24 h. After this period, the samples were placed in a desiccator to cool and prevent moisture absorption. The dry weight was measured on an analytical balance (precision: 0.001 g) after subtracting the weight of the porcelain crucibles. The gravimetric moisture content (GWC) (Eq. 1) of the horizons was determined by:

$$GWC\ (\%) = [(a - b)/b] \times 100, \quad (1)$$

where a is the mass of the wet sample (g), and b is the mass of the sample dried at 105 °C to constant weight (g).

Soil pH allows estimating H^+ ion concentration, which affects mineral availability (Teixeira et al., 2017). The pH of the soil horizons was measured with a portable pH meter fitted with a combined glass electrode. The samples were previously air-dried and sieved through a 2 mm mesh to obtain air-dried fine earth. Each sample was quartered, weighed, and divided into two 10 g portions in 150 mL glass beakers (soil: solution ratio 1:2.5). Then, 25 mL of distilled water was added to the first portion, and 25 mL of a saline solution (1 mol L^{-1} KCl) was added to the second.

Each sample was stirred for 60 seconds and rested for 1 hour. Afterward, the samples were stirred again, and pH readings were recorded with a portable electrode. Three readings per sample were averaged. ΔpH (Eq. 2) was calculated to estimate the sign of the net surface charge of the soil (negative for $\Delta pH < 0$, positive for $\Delta pH > 0$; Mekaru and Uehara, 1972):

$$\Delta pH = pH_{KCl} - pH_{H_2O}, \quad (2)$$

The total carbon contents were obtained by dry combustion in an elemental analyzer LECO® CHNS/O, model TruSpec Micro. 3.5 × 5 mm silver capsules were used, and the gases generated were quantified in an infrared detector at LIPEMVALE Laboratory, Federal University of the Jequitinhonha and Mucuri Valleys, Minas Gerais, Brazil. Five standards of known carbon composition were used to calibrate the equipment: soil 1 (C% = 3.35; code E11035 - A); soil 2 (C% = 0.732; code E11036–A); soil 3 (C% = 4.401; code E11037 – A); soil 4 (C% = 2.417; code E11038 – A) and soil 5 (C% = 0.141; code E11039 – A). The soil organic matter (SOM) content was calculated from the organic carbon content (C) using a standard conversion factor, assuming 58% of organic matter is carbon, yielding a Van Bemmelen factor of 1.724 (Van Bemmelen, 1890) (Eq. 3):

$$M.\ O\ (\%) = 100/58 \times C.\ O\ (\%) = 1.724 \times C.\ O\ (\%), \quad (3)$$

2.3 Magnetic analysis

Samples were collected at ~5 cm intervals throughout the trench depth (190 cm), yielding 26 samples during the drying season (DS) and 34 samples during the wetting season (WS). For this sampling, we used PIB-type acrylic boxes (2.0 x 2.0 x 2.0 cm). All samples were air-dried and sieved through a 2 mm mesh to obtain the air-dried fine earth fraction, subsequently pulverized using an agate mortar, quartered, and evaluated for magnetic properties, as detailed below. All environmental magnetism experiments were conducted at the Paleomagnetism and Rock Magnetism Laboratory of the Institute of Astronomy, Geophysics and Atmospheric Sciences, University of São Paulo, Brazil.

Magnetic susceptibility was measured using an MFK1-FA Multi-Function Kappabridge (AGICO Ltd.) at low frequency (χlf, $m^3\ kg^{-1}$) of 976 Hz and high frequency (χhf, $m^3\ kg^{-1}$) of 15,616 Hz, with a 200 A/m field. Mass-specific susceptibility was obtained by dividing volume susceptibility by the sample bulk density. Absolute frequency-dependent susceptibility was calculated as $\chi fd = \chi lf - \chi hf$ ($m^3\ kg^{-1}$), and relative frequency-dependent susceptibility was calculated as (Dearing et al., 1996a; Zhang et al., 2025) (Eq.4):

$$\chi fd\ (\%) = (\chi lf - \chi hf)/\chi lf/1.6 \times 100, \quad (4)$$

Thermomagnetic analysis was conducted to examine the relationship between magnetic susceptibility and temperature (κ vs. T). Approximately 0.20 g of powdered material was analyzed

using a CS-L cryostat (low temperature) and a CS-3 furnace (high temperature) coupled to a KLY-4 Kappabridge (AGICO Ltd.). Low-temperature (-194°C to 0°C) and high-temperature (0°C to 700°C) curves were obtained, with cooling curves recorded back to 0°C. The samples were heated in air at a rate of 7 °C min^{-1}, and the contributions of the empty furnace and temperature sensor were subtracted from all raw data using the Cureval software.

Magnetic hysteresis, isothermal remanent magnetization (IRM; acquisition and backfield curves) at room temperature, and First-Order Reversal Curve (FORC) analyses were performed using a Vibrating Sample Magnetometer (VSM; MicroMag 3900, Lake Shore Cryotronics), with a maximum applied field of 1 T. To ensure compatibility with the instrument measurement, ~0.20 g of each soil sample was packed into gel capsules and compacted with cotton to reduce noise. Hysteresis loops provided key parameters: saturation magnetization (Ms, A m^2 kg^{-1}), saturation remanent magnetization (Mrs, A m^2 kg^{-1}), and coercivity (Bc, mT). The loops were corrected for diamagnetic and paramagnetic contributions using the MicroMag AGM-VSM software. IRM analysis measured saturation isothermal remanent magnetization (SIRM; IRM_{1T}) (A m^2 kg^{-1}) and remanent coercivity (Bcr, mT). Parameters such as the S-ratio (Bloemendal et al., 1992), The high-coercivity minerals (HIRM) (A m^2 kg^{-1}) (Thompson and Oldfield, 1986), and substitute L-ratio (Liu et al., 2007) were used to distinguish low- and high-coercivity magnetic contributions. Here, S-ratio = 0.5 × (SIRM - IRM_{-300mT}/((SIRM)) (dimensionless), HIRM = 0.5 × (SIRM + IRM_{-300mT}) and substitute L-ratio = HIRM/ (0.5 × (SIRM + IRM_{-100mT}) (dimensionless), where IRM_{-100mT} and IRM_{-300mT} are the remanences remaining after applying backfields of 100 and 300 mT to the SIRM.

To obtain the FORC diagrams, we used an acquisition protocol comprising 200 reversal curves, a field increment of 1.02 mT, and an averaging time of 300 ms per point. The protocol specified a maximum smoothing parameter of 10 and 500 ms pauses at the calibration, saturation, and reversal fields. The saturation field was set to 500 mT, and the specified FORC diagram ranges were −40 to +40 mT for B_u and 0 to 100 mT for B_c. The acquisition time for each sample analyzed (DS, n = 3; WS, n = 6) was approximately 6 h 5 min 36 s. The raw data were processed and the FORC diagrams visualized using the open-source Python package FORCsensei (FORCaist/forcsensei: Release of FORCsensei| Zenodo) (Heslop et al., 2020).

The anhysteretic remanent magnetization (ARM) measurements were conducted in a magnetically shielded room with a horizontal SQUID Long-Core Magnetometer (2G Enterprises).

ARM was imparted with alternating-field (AF) peaks up to 100 mT and a 0.1 mT (≈79.6 A m^{-1}) direct current (DC) bias field, and ARM curves were obtained by increasing the AF peak stepwise (2, 4, 6, 8, 10, 12.5, 15, 17.5, 20, 22.5, 25, 27.5, 30, 35, 40, 45, 50, 60, 70, 80, 90, 100 mT). ARM susceptibility (χARM, m^3 kg^{-1}) (Eq. 5) was calculated by normalizing ARM by the DC bias field (H_{DC}, A m^{-1}) (Evans and Heller, 2003):

$$\chi_{ARM} = ARM/H_{DC}, \quad (5)$$

To identify the magnetic phases in a mixture of minerals in natural samples, the IRM and ARM acquisition curves of the soil and parent-material samples were decomposed into skew-normal coercivity components using MaxUnmix (Maxbauer et al., 2016b). From the decomposition, the following parameters can be determined: the mean coercivity of an individual grain population (Bh_{IRM}), the dispersion parameter (DP), defined as the standard deviation in logarithmic space, and the observed contribution (OC) of each component (Maxbauer et al., 2016b). We use the term median destructive field (MDF_{ARM}) for coercivity spectra derived from ARM curves to distinguish them from those derived from IRM curves, following Egli (2003).

An adaptation of the Cisowski-type test (1981), performed here on ARM curves (de Boer et al., 2001; Jaqueto et al., 2016; Mallett et al., 2025), was applied to 34 WS samples and a parent material sample. The stepwise AF demagnetization curves were obtained using the same sequence of field steps as for acquisition, as described above. The test provides two parameters: the fraction of saturation remanence at the crossover point (R) and the coercive field at which the curves intersect (H). In the original test, which compares IRM acquisition with AF demagnetization of SIRM, R = 0.5 is expected for noninteracting single-domain grains. This value is used here as a reference for comparison in the ARM-based test.

2.4 X-ray diffraction, Raman spectroscopy, and ATR-FTIR spectroscopy

The analyses were performed in laboratories at the University of Brasília (UnB). The mineralogy of the LVw and parent material samples was determined by X-ray diffraction (XRD). Mounts prepared from the bulk fractions (TOT) were analyzed using a Rigaku Ultima IV diffractometer equipped with a copper X-ray tube and a nickel filter, operated at a voltage of 35 kV and a current of 15 mA. Scans were performed over a 2θ range of 2–60°, at a scan rate of 5°

min^{-1} and a step size of 0.05°. Jade XRD 9.0 software, together with the Powder Diffraction File (PDF) database, was used to identify minerals based on their respective interplanar spacings (d).

Fourier transform infrared (FTIR) spectra were acquired using a Bruker Vertex 70 spectrometer operated in Attenuated Total Reflectance (ATR) configuration. An average of 96 scans was collected for each sample, with a spectral resolution of 4 cm^{-1}, over the 400 to 4000 cm^{-1} wavenumber range. Background spectra were recorded prior to each measurement to ensure baseline correction. Micro-Raman spectroscopy was performed using a LabRam HR Evolution spectrometer (HORIBA Scientific) equipped with a confocal microscope, a Charge-Coupled Device (CCD) detector, and an 1800 lines mm^{-1} diffraction grating. The system employed a 633 nm diode laser with an output power of approximately 1.7 mW, focused onto the sample using a 50× objective lens.

2.5 Extraction of the magnetic concentrate

The magnetic concentrate from the A horizon of the Lvw was obtained following the procedure described by Silva Filho et al. (2019). Initially, the samples were air-dried, gently disaggregated, and sieved through a 2 mm mesh to obtain the air-dried fine earth fraction. Subsequently, this fraction was dispersed in a 0.1 mol L^{-1} NaOH solution under low-speed mechanical stirring (50 rpm) for 16 h, according to Jackson (1969). Following dispersion, the sand fraction (2–0.05 mm) was separated by wet sieving, washed with distilled water, and oven-dried at 45 °C for 24 h. Finally, the magnetic concentrate was separated from the sand fraction using a hand-held permanent magnet.

2.6 Statistical analysis and data processing

Spearman's rank correlation coefficients were calculated among the magnetic parameters (Hu et al., 2020; Jaqueto et al., 2021) related to magnetic mineral concentration and grain size (χlf, χfd, χARM, and SIRM) to generate separate correlation matrices for the drying season (DS, n = 26) and wetting season (WS, n = 34).

In addition to the specialized software described above, original Python scripts were developed in Spyder 6 to process and visualize the other parameters.

3. Results

3.1 Soil properties and pH variations

The pH results (Fig. 2 b, c), based on samples grouped by period and horizon, revealed the acidic nature of the evaluated profile, common to *Latossolos* (Oxisol/Ferralsol) (Ker, 1997). In both seasons, the A horizon exhibited the lowest pH(H_2O) values.

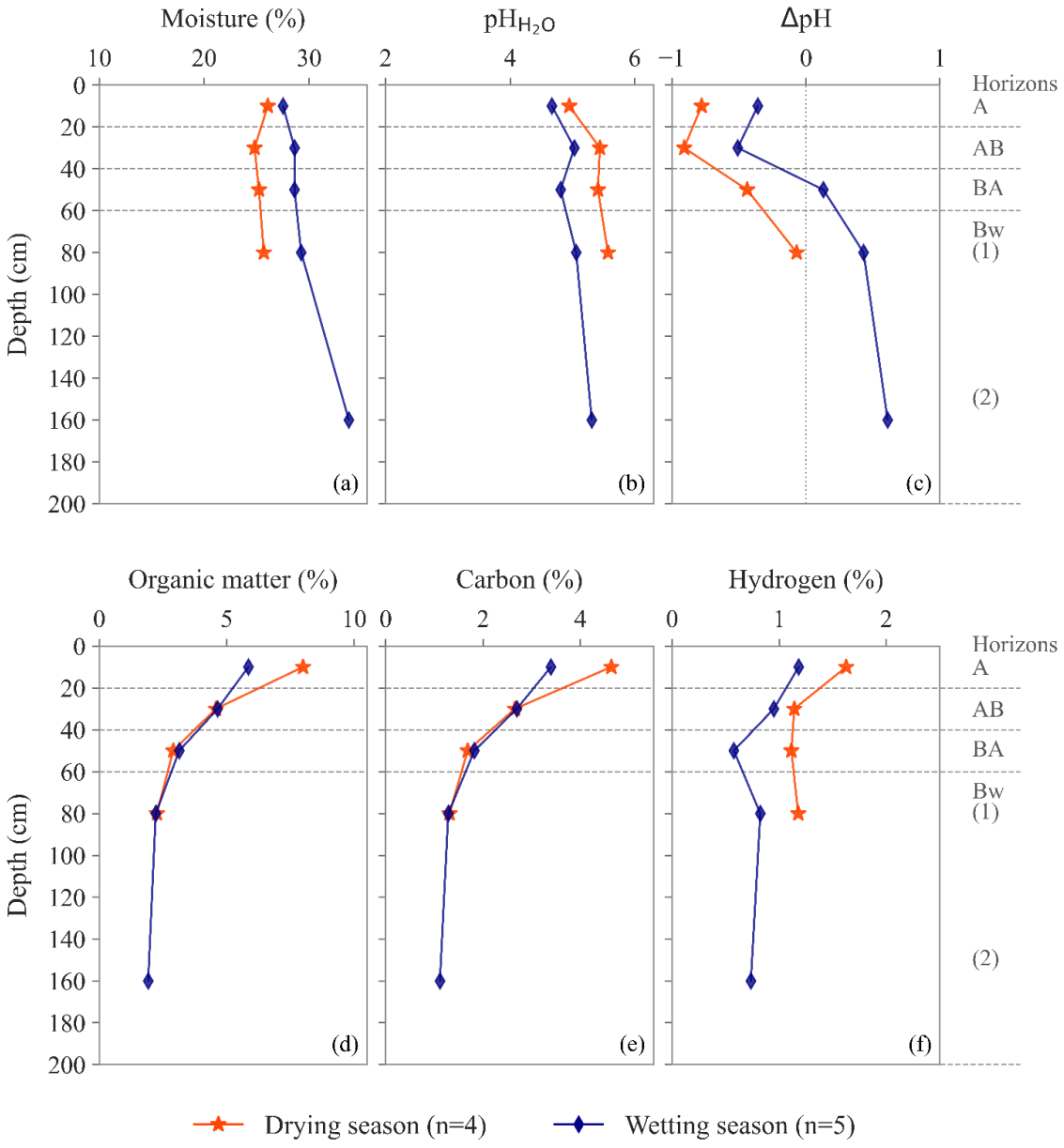


Figure 2. Measurements of moisture content (a), pH H_2O (b), ΔpH (c), organic matter (d), carbon (e), and hydrogen (f) in the horizons of the *Latossolo Vermelho* (Oxisol/Ferralsol) during the drying and wetting seasons.

In the wetting season (WS), the Bw horizon (60–190+ cm) exhibited a moisture (Fig. 2a) increasing profile depth (from 29.24% to 33.78%); therefore, Bw was subdivided into Bw1 and Bw2 during this period. A marked change in ΔpH (from 0.13 to 0.61) (Fig. 2c), indicates a net positive charge in the subsurface during the wetting season. These parameters following the highest percentages of organic matter, carbon, and hydrogen (Fig. 2d–f) in the A horizon (0–20 cm).

3.2 Magnetic properties

3.2.1 Magnetic susceptibility

During the drying season (DS) (Fig. 3 a), the χlf increase from the base to the top of the profile (from 127 × 10^{-8} m^3 kg^{-1} to 233 × 10^{-8} m^3 kg^{-1}) with a mean value of 194 × 10^{-8} m^3 kg^{-1}, with a standard deviation (σ) of ± 29 × 10^{-8} m^3 kg^{-1}. The wetting season (WS) show similar behavior to the DS, (from 119 × 10^{-8} m^3 kg^{-1} to 223 × 10^{-8} m^3 kg^{-1}, with a mean of 196 × 10^{-8} m^3 kg^{-1} and σ ± 24 × 10^{-8} m^3 kg^{-1}). The highest χfd value (Fig. 3 b) (47 × 10^{-8} m^3 kg^{-1}) was recorded at 30–35 cm depth (AB horizon) during the drying season.

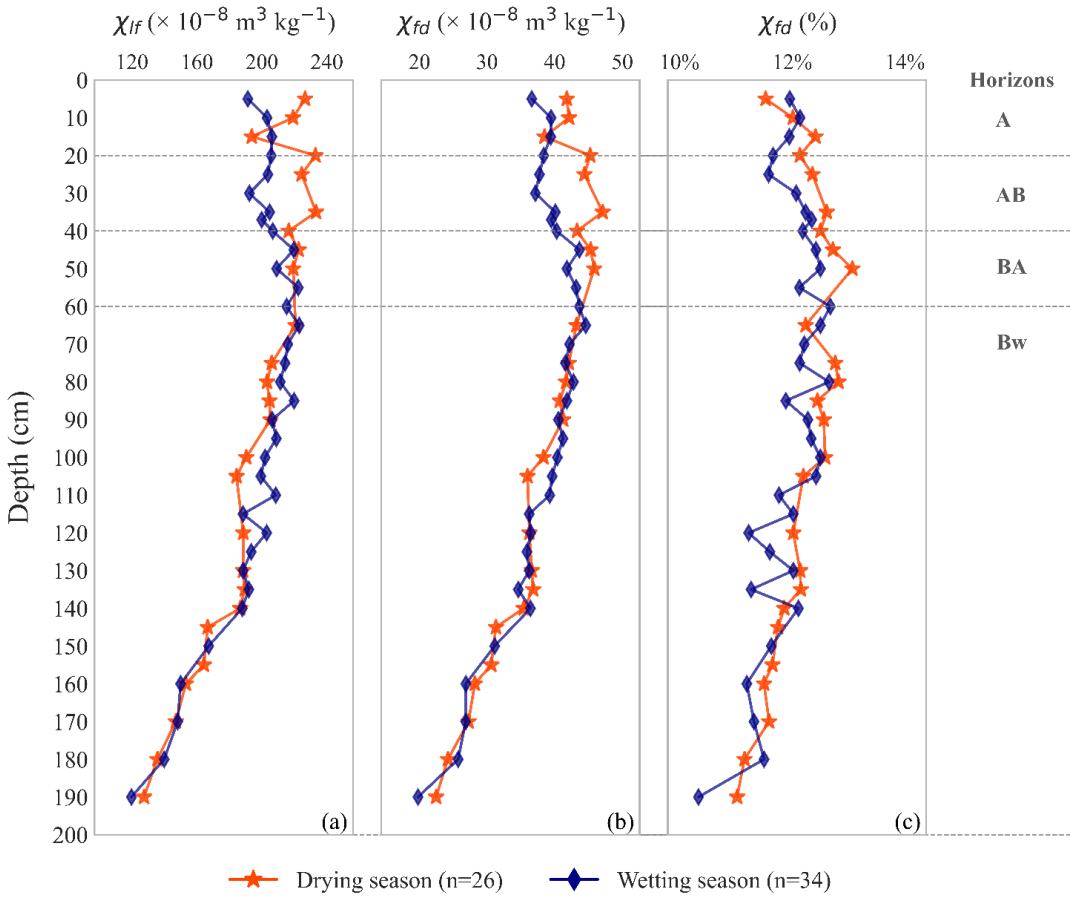


Figure 3. Magnetic susceptibility measurements χlf (m^3 kg^{-1}) (a), χfd (m^3 kg^{-1}) (b), χfd (%) (c), estimated for the drying and the wetting season.

The χfd (%) parameter, which reflects the relative contribution of superparamagnetic grains to the bulk susceptibility (Dearing et al., 1996a), in the drying season is higher at a depth of 50–55 cm (BA horizon), 13.07 %, and is lower at the greatest depth 185–190 cm (11.02 %) (Fig. 3 c). The mean for this period was 12.15% ± 0.51%. The same trend in χfd (%) (Fig. 3c) was observed for wetting season, with a maximum of 12.67%, a minimum of 10.34%, a mean of 11.96%, and σ ± 0.50% in these samples.

3.2.2 Thermomagnetic analysis

A consistent thermomagnetic behavior was observed in the upper soil horizons for both periods, characterized by an enhancement in the χ signal near −163 °C (~110 K) (Fig. 4 a; SFig. 2). In the wetting season no enhancement was observed at the base of the profile (Fig. 4b), which displayed predominantly paramagnetic behavior.

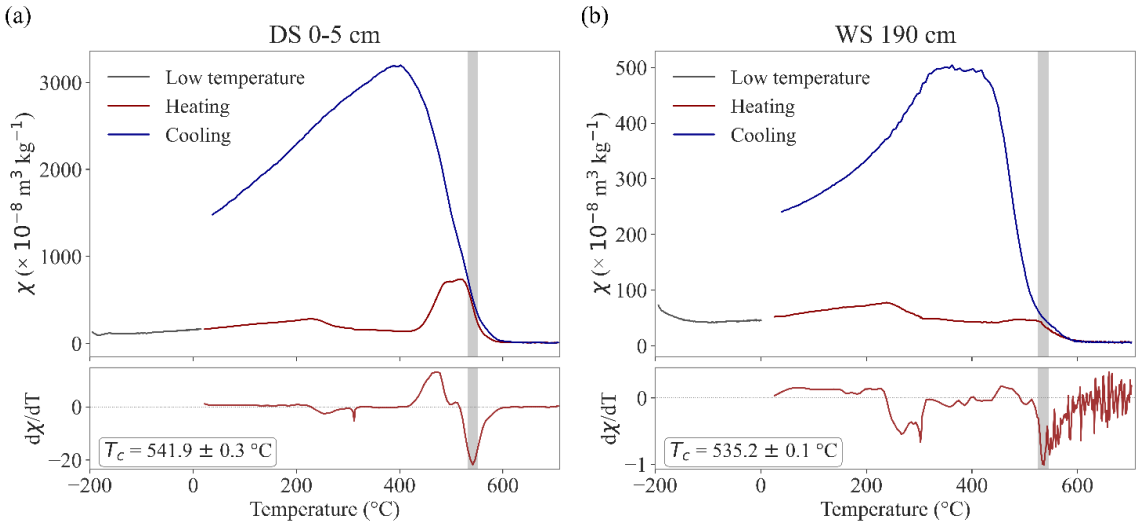


Figure 4. Low- and high-temperature thermomagnetic curves measured at profile depth for a DS sample (0-5 cm) (a) and a WS sample (190 cm) (b).

The thermomagnetic curves during heating for soil samples in both seasons (Fig. 4a, b; SFig. 2) are similar, showing a gradual increase in χ up to 228–240 °C, followed by a drop around 400 °C. Another increase in χ occurs between 480–526 °C, followed by an abrupt drop at ~550 °C on average. After this final drop, χ decreased gradually to the Néel temperature of hematite at ~680–690 °C (Jordanova and Jordanova, 2016a; Muxworthy et al., 2023). All evaluated samples presented irreversible mineralogical transformations, evidenced by a marked increase in χ during cooling.

3.2.3 Hysteresis, IRM, and FORC

In general, the samples from both periods (SFig. 3 a, c) exhibited narrow, slightly wasp-waisted shapes, low coercivity, a slight inflection near the 200 mT field, and a tendency toward saturation at low fields (Fig. 3 b, d). During the drying season, the mean Ms (Fig. 5 a) across the profile measurement depths was 71.44 × 10^{-3} A m^2 kg^{-1}, with a maximum of 138 × 10^{-3} A m^2 kg^{-1} (30–35 cm) and σ ± 23.63 × 10^{-3} A m^2 kg^{-1}. In wetting season samples, the maximum Ms value was recorded at 65–70 cm depth (147.8 × 10^{-3} A m^2 kg^{-1}), with a mean of 81 × 10^{-3} A m^2 kg^{-1} and a lower σ ± 19.42 × 10^{-3} A m^2 kg^{-1}.

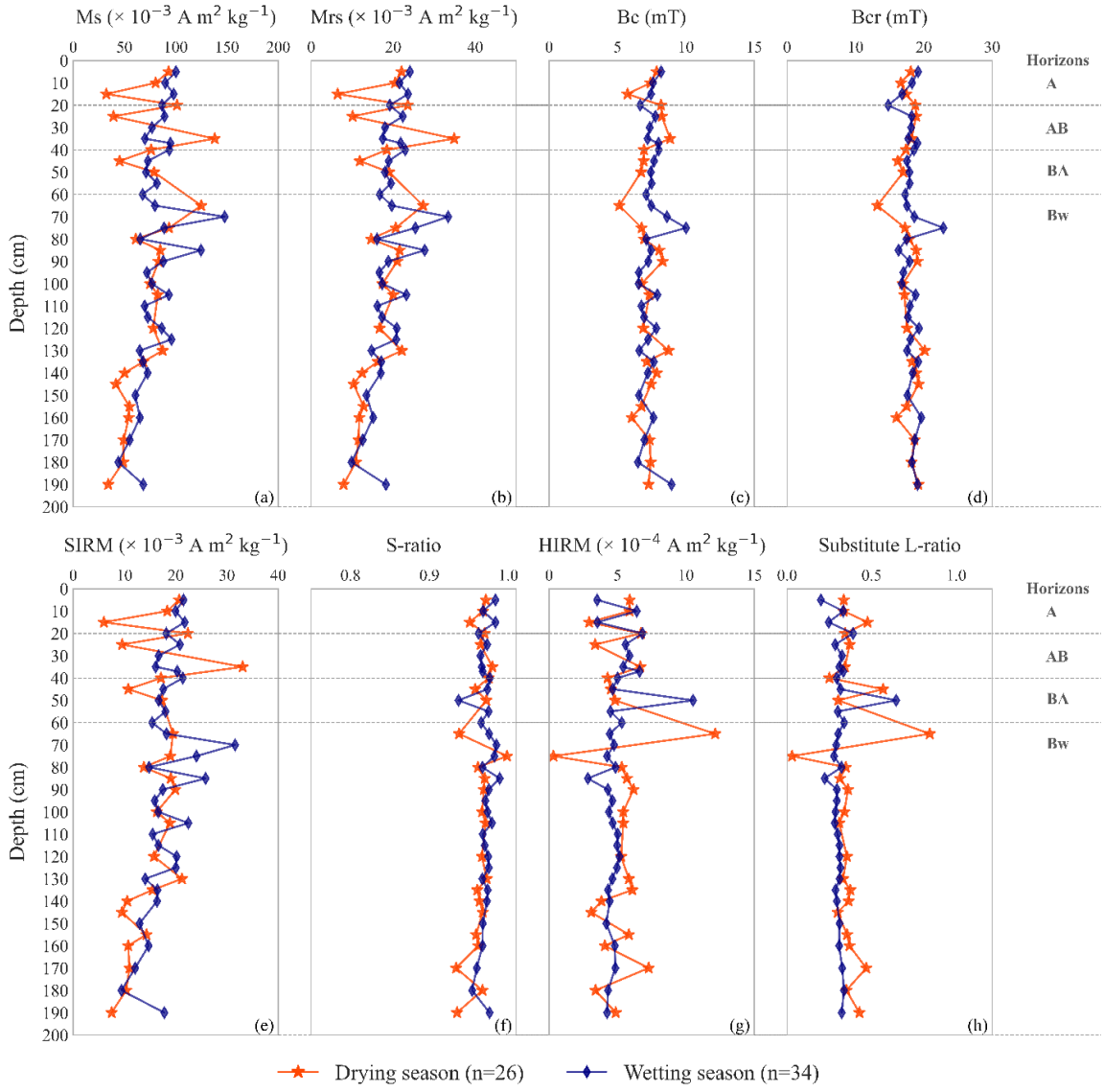


Figure 5. Parameters derived from hysteresis loops (a, c) and isothermal remanent magnetization (IRM) curves (b, d–h) estimated for the drying and the wetting season.

Coercivity-related parameters (Bc and Bcr) (Fig. 5c, d) exhibited lower variation across the profile, possibly due to a homogeneous grain-size distribution in the samples. Estimated Bc values (Fig. 5c) were relatively low, ranging from 5.14 to 8.85 mT, with a mean of 7.28 (± 0.87 mT) for DS samples. The same Bc trend was observed for WS samples, which showed a minimum value of 6.49 mT at 175–180 cm depth and a maximum of 10.02 mT (70–75 cm). The mean Bc (7.46 ± 0.74 mT) in the WS was slightly higher, with a lower deviation.

The S-ratio parameter (Fig. 5 f) showed little variability across the profile and between evaluated periods. In the DS it ranged from 0.93 to 1.00, with a mean of 0.96 (± 0.013). Similar values occur in the WS (between 0.94 and 0.99 with mean of 0.97 (± 0.01)). The HIRM parameter (Fig. 5 g), with reported the more coercive minerals in minute concentrations. For the drying season was 5.20×10^{-4} ($\pm 2.02 \times 10^{-4}$ A m² kg^{-1}), and for wetting season was 4.96×10^{-4} ($\pm 1.26 \times 10^{-4}$ A m² kg^{-1}). In the drying season, the substitute L-ratio (Fig. 5h) presented a mean value of 0.37 (± 0.13), ranging from 0.03 to 0.84. For the wetting season, this parameter has lower variation, with a mean of 0.31 (± 0.06) and depth values ranging from 0.20 to 0.64.

The Mrs/Ms and Bcr/Bc ratios, which vary as a function of grain size, were plotted on the Day diagram modified by Dunlop (Day et al., 1977; Dunlop, 2002a, b) (Fig. 6). It shows discrete ration variations suggesting that the magnetic grains follow a similar size distribution along the profile and between evaluated seasons, clustering in the pseudo-single-domain (PSD) region.

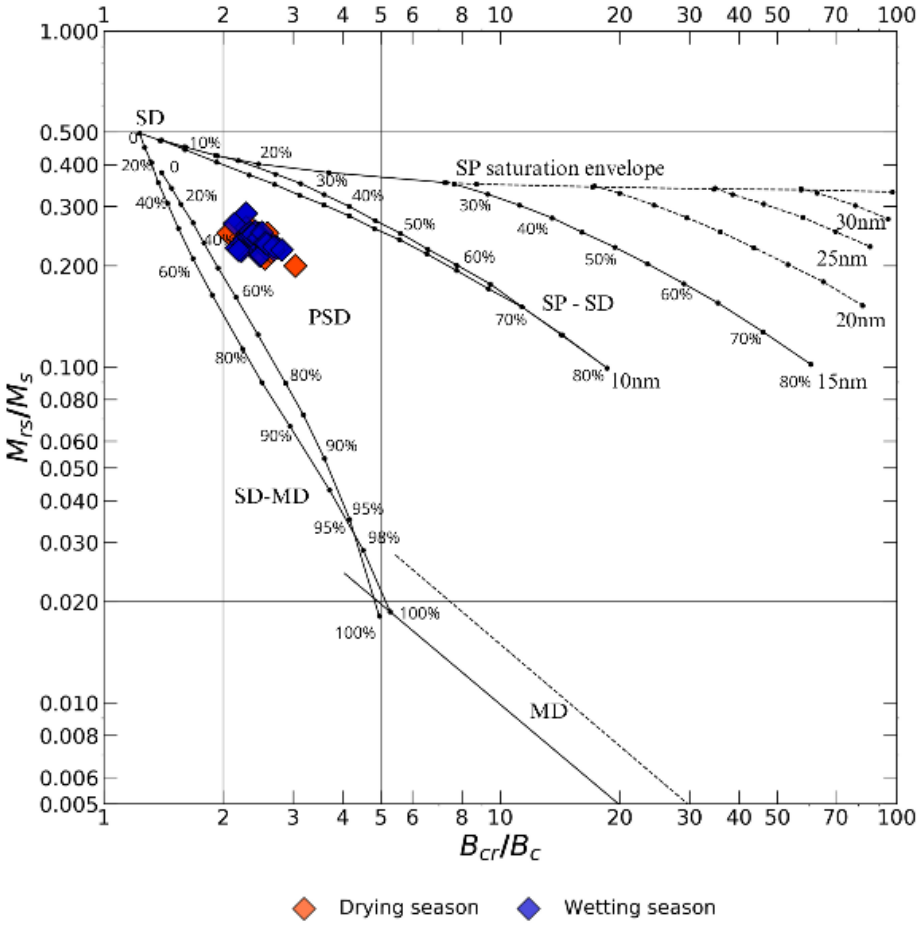


Figure 6. Day diagram (1977) modified by Dunlop (2002a) to characterize the domain state of the magnetic particles present in the DS and WS samples.

The coercivity distributions and local interactions between magnetic particles in (Fig. 7 a, b; SFig. 4) show distributions peak at low coercivity (Bc ≈ 8–10 mT). The FORC diagrams (Roberts et al., 2000) show two main features: a narrow central ridge along Bu = 0 extending to Bc ≈ 50–60 mT, which is diagnostic of non-interacting SD particles (Egli et al., 2010), and a broader, vertically spread contribution at Bc < 20 mT, typical of vortex-state and thermally activated particles near the SP/SD threshold (Roberts et al., 2014). Thus, these FORC diagrams indicate a mixture of non-interacting SD and vortex-state (PSD) particles, consistent with the Day diagram.

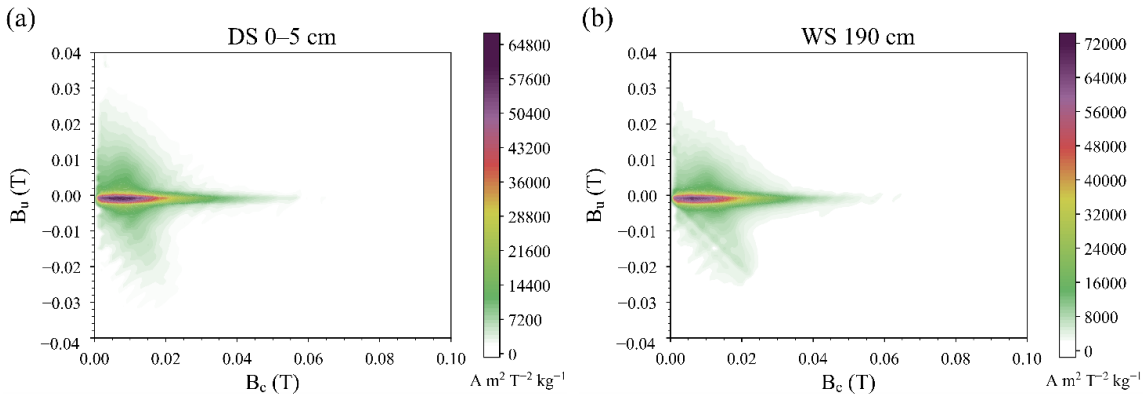


Figure 7. First-order reversal curve (FORC) diagrams for a DS sample (0-5 cm) (a) and a WS sample (190 cm) (b).

3.2.4 ARM curves

The ARM acquisition ranged from 65.68 to 181.98 × 10^{-5} A m² kg^{-1} with a mean of 137.66 × 10^{-5} A m² kg^{-1}, considering both periods (Fig. 8b and SFig. 5 a, b), demonstrate the dominance of the low-coercivity magnetic fraction, with saturation at fields < 30 mT. These values show no systematic difference between the periods, whereas ARM intensity decreased with depth.

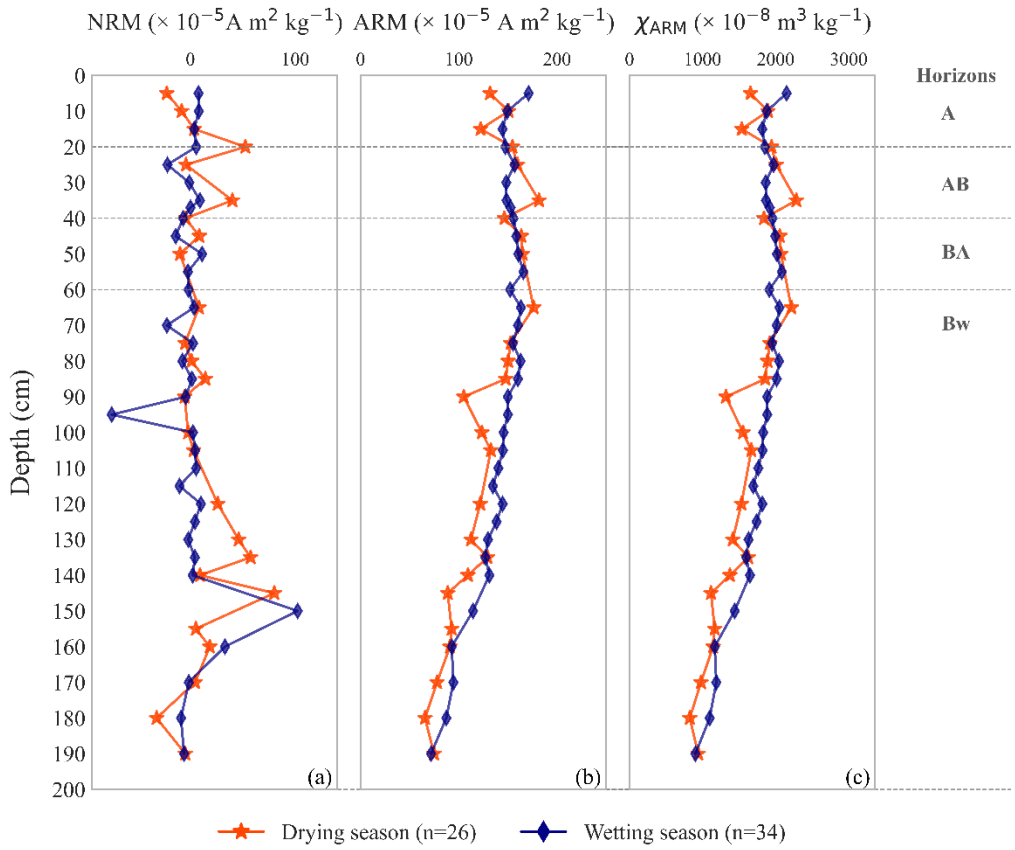


Figure 8. Results by period of: (a) Natural Remanent Magnetization (NRM), (b) acquisition of Anhysteretic Remanent Magnetization (ARM), and (c) Susceptibility of Anhysteretic Remanent Magnetization (χARM).

The χARM parameter (Fig. 8c), sensitive to the fine ferrimagnetic fraction, decreased from the top to the base of the profile in both seasonal periods, varying between 825.31 and 2286 × 10^{-8} m^3 kg^{-1} (mean of 1695.09 × 10^{-8} m^3 kg^{-1}). However, a greater variation was observed in natural remanent magnetization (NRM) (0 mT) (Fig. 8 a) between periods, although unrelated to depth, with a maximum of 192.78 × 10^{-5} A m^2 kg^{-1}, minimum of 2.60 × 10^{-5} A m^2 kg^{-1} and mean of 36.88 × 10^{-5} A m^2 kg^{-1} in DS and 30.97 × 10^{-5} A m^2 kg^{-1} in WS.

In the Cisowski-like test (1981) (SFig. 6 b, d), the H value for the mineralogical assemblage is low, recording values from 12.67 to 14.09 mT (mean = 13.43 ± 0.35 mT) across the profile. The curves in WS show symmetric behavior, with R values between 0.5 and 0.55 (mean = 0.51 ± 0.01). This indicates that remanence in the soil profile is dominated by a non-interacting single-domain

grain fraction (de Boer et al., 2001; Jaqueto et al., 2016; Mallett et al., 2025), confirming the FORC diagrams.

3.2.5 Unmixing of IRM and ARM curves

The unmixing of mineral phases in the samples was performed from IRM and ARM acquisition curves (Fig. 9 a–d) for DS (n=26) and WS (n=34) samples. However, samples exhibiting excessive noise in the derivative of magnetization with respect to the logarithm of the applied magnetic field (dM/dlog(B)) were excluded from the statistical analysis.

In the LVw profile, two IRM coercivity spectra were identified (Fig. 9 b): a low-coercivity (or first) component (C1 - blue line) and a high-coercivity (or second) component (C2 - purple line). Between seasons, C1 showed Bh_{IRM} variations of 14.63-27.94 mT, with a mean of 20.90 mT (1.31 log_{10} units) and a mean dispersion parameter (DP_{IRM}) of 0.30 (log_{10} units), representing the dominant fraction in IRM acquisition (mean OC: 72%). The magnetically more coercive fraction (C2) exhibited Bh_{IRM} values between 91.76 and 549.57 mT, with a mean value of 231.85 mT and a lower, invariant contribution, as indicated by a mean OC of 28%. C2 showed greater DP_{IRM} in both seasons, with a mean value of 0.67 (log_{10} units).

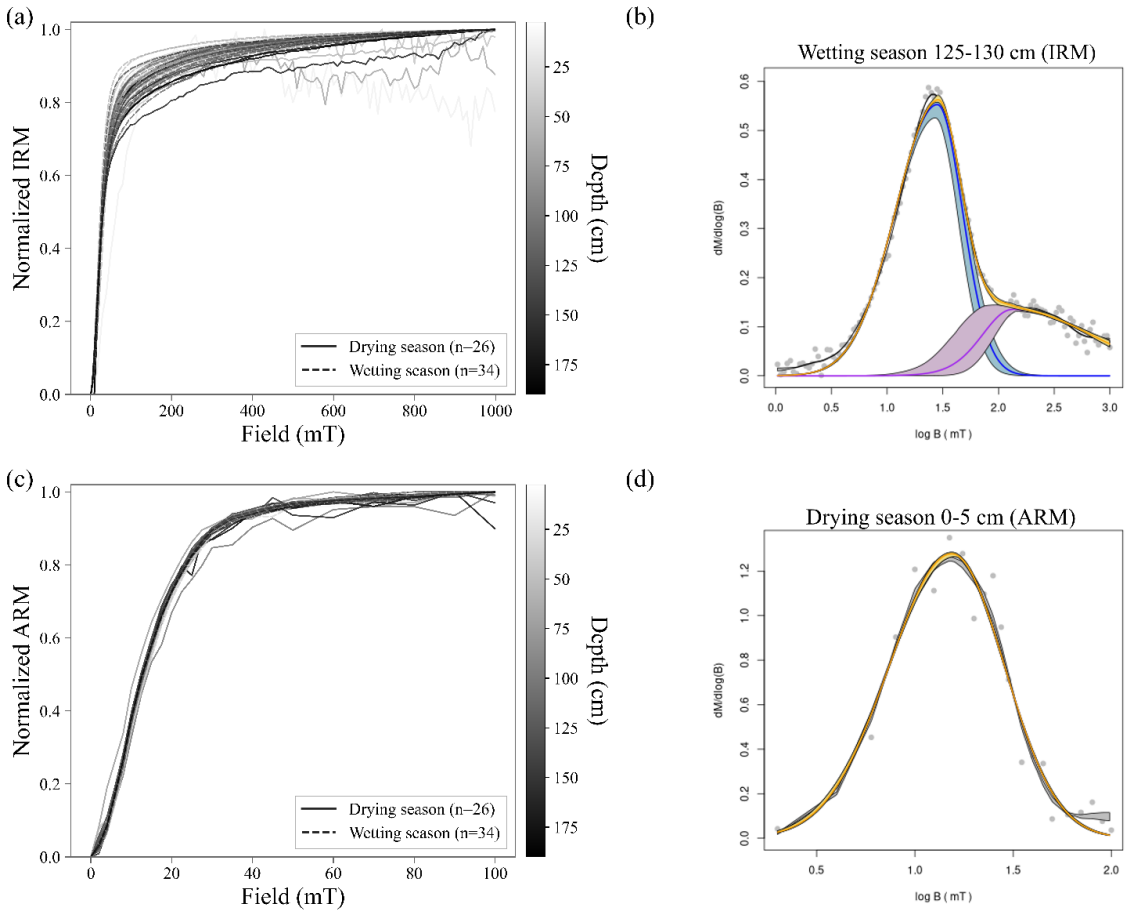


Figure 9. Normalized Isothermal Remanent Magnetization (IRM) (a) and Anhysteretic Remanent Magnetization (ARM) (c) acquisition curves; example of the decomposition of coercivity spectra for IRM WS (125-130 cm) sample (b) and ARM DS (0-5 cm) sample (d) curves using the MaxUnmix software.

The plot proposed by Egli (2004a, 2004b) was used to assist in identifying the potential origin of the magnetic carriers responsible for the remanent magnetization acquired by the soil and parent material samples. In this case, modeling was developed for a single coercivity component for LVw samples, as shown in the example (Fig. 9d) and results (Fig. 10).

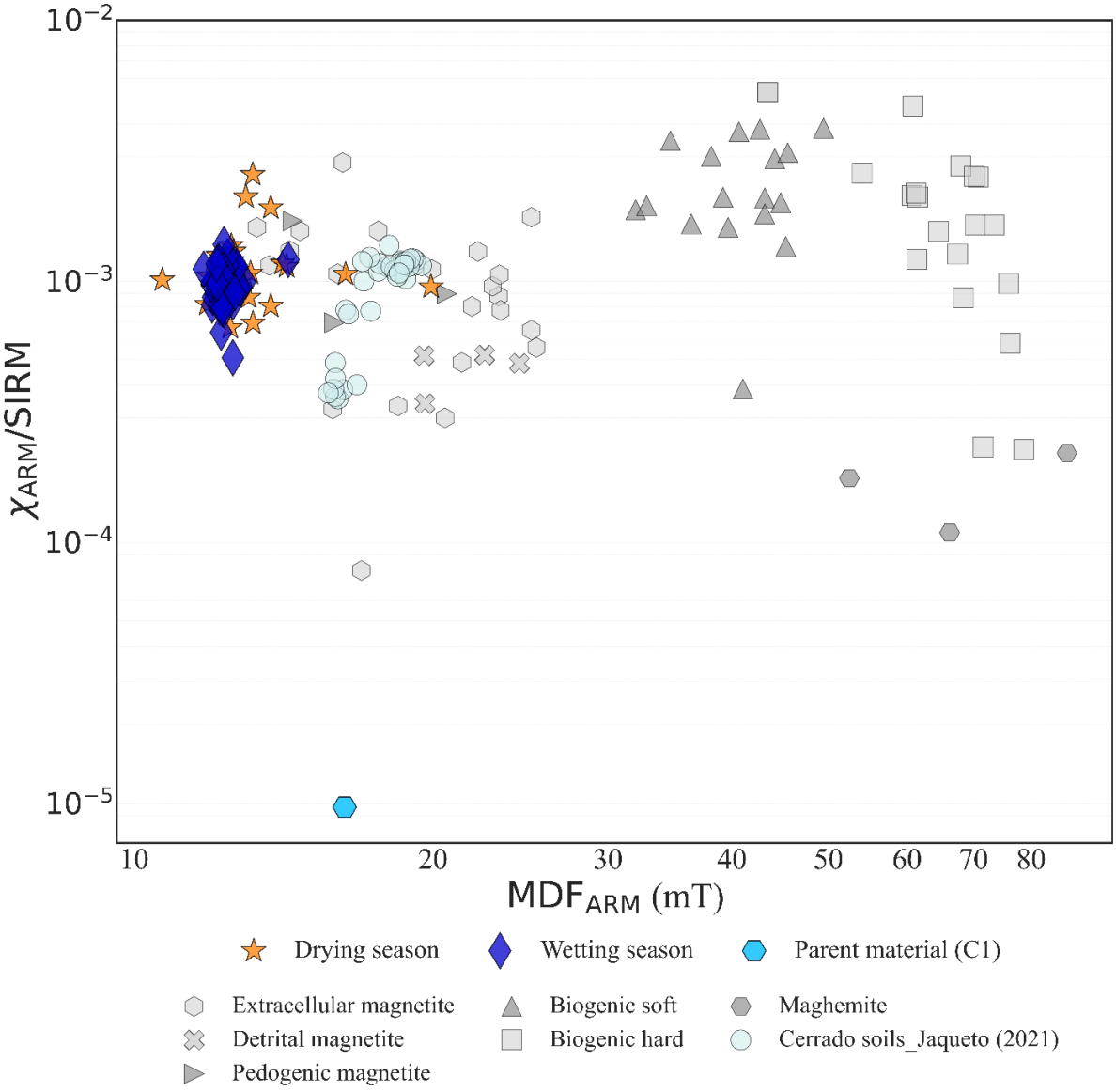


Figure 10. Biplot of χARM/SIRM versus the median coercive field of the ARM acquisition curves (MDF_{ARM}), obtained with the MaxUnmix software (Maxbauer et al., 2016b), to identify the origin of the components carrying the remanent magnetization in the soil samples evaluated during the DS (n = 26) and the WS (n = 34), and in the parent material sample (low-coercivity component 1). Secondary data used for comparison were obtained from Egli (2004a), Egli (2004b), and Jaqueto et al. (2021).

The MDF_{ARM} parameter averaged 13.12 mT (± 1.73) in DS and 12.43 mT (± 0.42) in WS. Mean DP_{ARM} values were 0.35 (± 0.037 log) in DS and 0.34 (± 0.011 log) in WS. In both periods, soil samples clustered near coercivity ranges associated with extracellular, pedogenic, and detrital magnetite.

3.3 Magnetic properties of the parent material

The magnetic properties of the slate parent material (Table 1 and SFig. 7 (a–f)) show the χlf result is close to the signal of unweathered slates under tropical conditions (χlf 6×10^{-8} m^3 kg^{-1}) pointed out by Preetz et al. (2017), but lower than the value estimated for weathered slates (15×10^{-8} m^3 kg^{-1}). Furthermore, an identical χfd value was reported by those authors for unweathered samples (χfd 0.4×10^{-8} m^3 kg^{-1}). Despite the greater similarity, the slate sample the color changes from greenish-grey to reddish-purple tones (Campos et al., 2013), indicate signs of weathering.

Table 1. Magnetic properties of the parent material.

χlf (m^3 kg^{-1})	6.22×10^{-8}
χfd (m^3 kg^{-1})	0.40×10^{-8}
χfd (%)	3.95
Ms (A m^2 kg^{-1})	15.40×10^{-3}
Mrs (A m^2 kg^{-1})	12.37×10^{-3}
SIRM (A m^2 kg^{-1})	12.03×10^{-3}
Bc (mT)	295.56
Bcr (mT)	356.94
S-ratio (dimensionless)	0.40
HIRM (A m^2 kg^{-1})	72.57×10^{-4}
Substitute L-ratio (dimensionless)	0.63
NRM (A m^2 kg^{-1})	2.64×10^{-5}
$ARM_{100\ mT}$ (A m^2 kg^{-1})	0.93×10^{-5}
χARM (m^3 kg^{-1})	11.65×10^{-8}

Thermomagnetic curves of the parent material (SFig. 7 d) showed a weak, noisy signal, limiting the identification of potential magnetic transitions and warranting caution in interpreting thermal treatment. Thus, clear evidence of Verwey or Morin transitions was not observed, and magnetite/hematite presence could not be confirmed via low-temperature curves. At high temperatures, the heating curve showed a progressive increase in susceptibility up to ~552 °C, followed by a reduction near 653 °C. The low Ms and S-ratio values, associated with high Bc and Bcr values (Table 1), suggest the predominance of a high-coercivity magnetic mineral, confirmed by IRM curve decomposition showing Bh_{IRM} of 529 mT and DP of 0.33 (log_{10} units) (SFig. 7 f).

In the parent material, parameters derived from the Cisowski-like test (SFig. 7c) were higher than in the soil samples, with H = 65.78 mT and R = 0.53, suggesting a larger remanence fraction persists at the cross-over point of the higher-coercivity parent-material curve. This greater remanence stability makes the demagnetization step less efficient than in the non-interacting SD assemblage observed for the soil samples.

It was not possible to decompose the ARM acquisition curve of the parent material into a single (mean) coercivity spectrum, as was done for the soil samples. Instead, the parent material showed a clear separation of the coercivity spectrum into two components (SFig. 7 e). Component MDF_{ARM} (C1), represented by the blue line and included in Fig. 10, showed the lowest coercivity, 16.29 mT (± 1.73 mT), close to values estimated for the soil samples, with a log DP_{ARM} (C1) of 0.40 (log_{10} units) and OC (C1) of 29%. The second component (MDF_{ARM} (C2)), represented by the purple line, dominated the ARM acquisition of the sample, with OC (C2) of 71%, MDF_{ARM} (C2) of 130 mT, and DP_{ARM} (C2) of 0.28 (log_{10} units). This component is probably associated with a higher-coercivity magnetic mineral phase and/or a higher degree of oxidation.

3.4 Mineralogical characterization (XRD, Raman, and ATR-FTIR)

3.4.1 XRD

The mineral composition of the A horizon contains quartz (Qz), kaolinite (Kln), and hematite (Hem), maghemite (Mgh) and gibbsite (Gbs), whereas illite (Ilt)/muscovite (Ms) was observed in the parent material (Fig 11 a, b). Although we assigned the magnetic mineral present in the samples to maghemite (which may have been the main contributor to the observed reflection owing to the degree of particle oxidation), it is difficult to distinguish this phase clearly from

magnetite because of overlapping diffraction reflections associated with their similar interplanar spacings (Fontes et al., 2000; Camêlo et al., 2018). For the same reason, illite could not be distinguished from muscovite in the parent material based on analysis of the bulk sample.

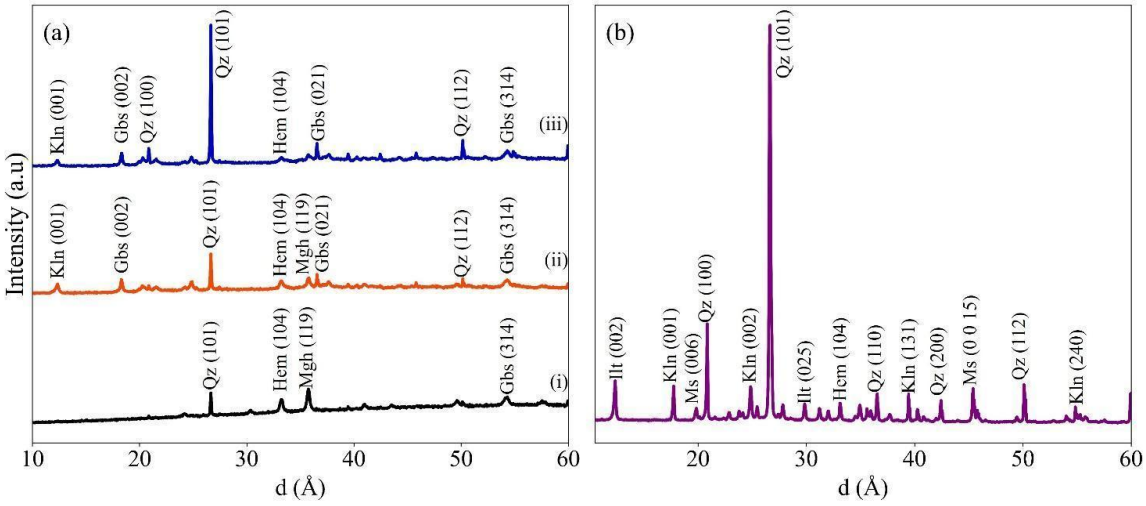


Figure 11. X-ray diffractometry (XRD) (a) patterns of: (i) concentrate of magnetic particles from the A horizon of the LVw, (ii) sample of the A horizon of the LVw during the drying season, (iii) sample of the A horizon of the LVw during the wetting season; and XRD pattern of the parent material sample (b).

3.4.2 Raman and ATR-FTIR spectroscopy

The FTIR-ATR spectra obtained for the LVw samples (Fig. 12 a (ii, iii, iv)) and the parent material (Fig. 12 a (v)) showed higher intensity in the absorption bands at 420, 466, 530, 740, 794, 914, 1006, 1032, and 1118 cm^{-1}. In addition, two other absorption bands (694 and 826 cm^{-1}) were identified in the parent material spectrum. The bands between 400 and 600 cm^{-1} is diagnostic for iron oxides because it reflects Fe–O bond vibrations. The band at 420 cm^{-1} possibly represents Fe–O stretching but, on its own, may not be diagnostic of a single mineral phase, since this interval can be assigned to either hematite, at 420 cm^{-1} (Opris et al., 2025), or maghemite, at 430 cm^{-1} (Namduri and Nasrazadani, 2008).

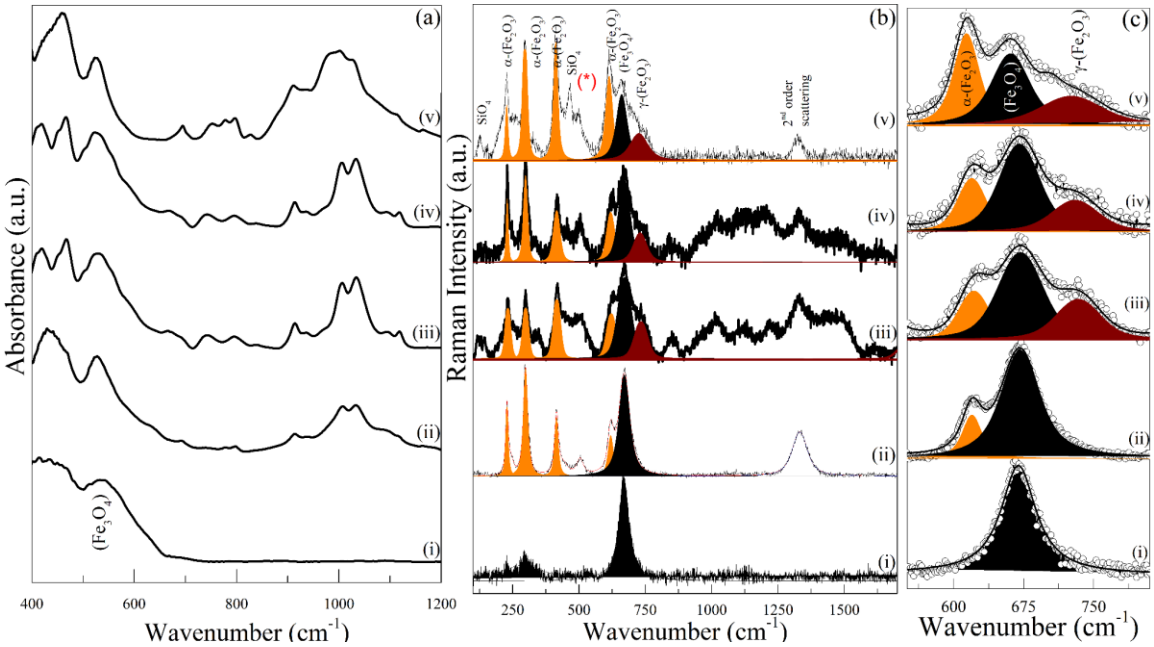


Figure 12. FTIR-ATR (a), Raman spectroscopy (b), and Raman spectrum deconvolution (c). Samples: (i) natural magnetite sample (standard), (ii) concentrate of magnetic particles, (iii) sample of the A horizon of the LVw during the drying season, (iv) sample of the A horizon of the LVw during the wetting season, and (v) parent material.

The absorption bands at 466 and 530–540 cm^{-1} are characteristic of hematite (Namduri and Nasrazadani, 2008; Reethu et al., 2023). Although the most intense FTIR band of magnetite is reported around 570 cm^{-1} (Salama et al., 2015; Namduri and Nasrazadani, 2008), both the soil samples and the magnetite standard measured on a natural sample showed absorption peaks at 530 and 528 cm^{-1}, respectively. However, these bands overlap with strong kaolinite (Si–O–Al, ~535 cm^{-1}; Si–O bending, ~470 cm^{-1}) and quartz absorptions; FTIR assignments of Fe oxides in these bulk samples are therefore tentative and are used here only in combination with the XRD, Raman and magnetic data. The characteristic bands of quartz were observed at 795 cm^{-1} (Si–O), and of kaolinite at 914 cm^{-1} (Al–O–H), 1006 cm^{-1} (Si–O–Al), and 1032 and 1118 cm^{-1} (Si–O–Si bond) (Reethu et al., 2023).

The deconvolution of the Raman spectroscopy results (Fig. 12 b) using the Peakfit® software with Lorentzian functions (Fig. 12 c) allowed the identification of the characteristic bands of magnetite (Fe_3O_4) at 670 cm^{-1} (A1g mode); hematite (α-Fe_2O_3), at 225 cm^{-1} (A1g), 290–300 cm^{-1} (Eg mode), 412 cm^{-1} (Eg), 497 cm^{-1} (A1g), and 612 cm^{-1} (Eg); and maghemite (γ-Fe_2O_3),

with its highest intensity in the band at 726 cm^{-1} (Eg mode) (Oh et al., 1998; Hanesch, 2009). The band at 127 cm^{-1} in the E (TO+LO) mode and the band at 467 cm^{-1} in the A1 mode (Krishnamurti, 1958), confirmed by the presence of quartz.

The broader band in the region between 670 and 730 cm^{-1} in the soil and parent material samples, which suggests a mixture and co-occurrence of both ferrimagnetic phases (magnetite and maghemite), reflecting the degree of oxidation of the particles. Moreover, the absence of intensity in the band at 730 cm^{-1} in the magnetic concentrate sample (obtained after clay dispersion with 0.1 mol L^{-1} NaOH) suggests that maghemite occurs preferentially in the clay fraction of the soils (Kämpf et al., 2009), and that the intensities at ~670 cm^{-1} in all samples are more likely to reflect magnetite. Otherwise, other characteristic maghemite bands (~665 and 1330 cm^{-1}) (Hanesch, 2009) would also be absent from the magnetic concentrate sample. Likewise, the intensity at ~1221 cm^{-1} corresponds to hematite (Oh et al., 1998), related to the two-phonon (2LO) scattering mode (Marshall et al., 2025).

Since the parent material and the soil materials are natural samples of mixed composition; it is possible that the additional bands characteristic of magnetite (310 and 540 cm^{-1}) were masked by stronger bands of other iron oxides, as hematite and maghemite (Hanesch, 2009; Schwaminger et al., 2017). Another pertinent observation concerns the degree of crystallinity of hematite. According to Marshall et al. (2025), decreasing crystallinity of this mineral makes its bands broader, resulting in a shift of the wavenumber toward lower values, in addition to the absence of intensity near 244 cm^{-1} (EgT) in massive and nanoparticulate hematite samples. This band is absent from all Raman spectra obtained. Finally, because laser heating can oxidize magnetite to maghemite and hematite (Hanesch, 2009), the relative intensities of the Fe-oxide Raman bands should be interpreted with caution. Accordingly, no single technique is used here as definitive evidence for magnetite or maghemite; the combined XRD, Raman and magnetic data are best described as indicating a fine-grained magnetite–maghemite assemblage, probably spanning different oxidation states.

4. Discussion

4.1 Soil properties

The higher acidity in the surface horizons may be related to greater interaction with organic matter and to the intense microbial activity associated with the plant root zone (Ritchie and Dolling, 1985; Stumm and Sulzberger, 1992). On the other hand, the greater moisture at the base of the profile (Fig.2 a) may result from an increased proportion of micropores in the soil aggregates, as estimated by Campos (2009). During the wetting season (WS), pH_KCl values higher than those determined in H_2O on the subsurface horizons indicate the development of net positive charges (Fig.2 c), a condition compatible with the acric character of the profile and its greater affinity for anions. The lower pH(H_2O) in the WS (Fig.2 b) may indicate seasonal acidification, which, if accompanied by changes in redox conditions, could increase Fe mobility.

According to Schwertmann (1985), the relative proportion between hematite and goethite reflects soil moisture conditions, the rate of Fe release from the parent material, pH, and soil organic matter content. Although slightly lower pH values and humidity could favor goethite formation, especially in the approximate pH range of 4 to 6, the profile evaluated has good drainage capacity and remains under predominantly aerobic conditions during much of the seasonal cycle. Good oxygenation of the pore spaces, together with tropical conditions, may favor the formation and preservation of hematite, in agreement with the mineralogical results. No evidence of goethite was observed with the techniques used in the present study.

4.2 Thermal and compositional signatures of the magnetic minerals

The low-temperature thermomagnetic curves of the soil samples showed an increase in χ near −163.15 °C (110 K) (Fig. 4 and SFig.2), which may be related to the Verwey transition (Tv) of magnetite. In stoichiometric magnetite, Tv occurs at ~120 K (Verwey, 1939). Because the low-temperature curves were measured before any heating, this feature reflects the original mineralogy of the samples.

The shift of Tv to temperatures below −153 °C may result from deviations from stoichiometry, partial oxidation of the particles, isomorphic substitutions, or defects in the crystal structure. These factors may also weaken or completely suppress the expression of the transition (Özdemir et al., 1993). Thus, the suppression of Tv observed at the base of the profile, at a depth

of 190 cm during the WS (Fig. 5 b), may indicate a greater degree of oxidation or non-stoichiometry of magnetite, although a lower concentration of the mineral could also reduce the intensity of the transition. Additionally, the increase in χ values near −13 °C (260 K) identified in the curves of samples from both periods and is possibly related to the Morin transition of hematite. However, fine-grained and Al-substituted pedogenic hematite commonly lacks a Morin transition (Özdemir et al., 2008), so this feature more likely reflects coarser hematite, possibly inherited from the parent material.

In the high-temperature thermomagnetic curves, χ increased from room temperature to approximately 230 °C (Fig. 4 and SFig.2). This behavior may indicate progressive changes in the blocking state of the finest SD particles, which begin to show SP-like behavior during heating, as well as of the onset of thermally induced mineralogical transformations (Gao et al., 2019). Between 230 and 400 °C, all samples showed a reduction in χ. This behavior is compatible with the transformation of maghemite, a metastable phase during heating, into hematite, which has a weaker magnetic response (Dunlop and Özdemir, 1997; Liu et al., 2005).

In the heating curves (Fig. 4 and SFig.2), a distinction must be made between phases present in the untreated samples and phases produced during the κ–T experiment, because all curves are strongly irreversible. The pronounced χ increase above ~480–520 °C, followed by a sharp decrease at ~550–580 °C, occurs in the temperature range in which new magnetite is commonly produced during heating from Fe-bearing clay minerals and Fe oxides, particularly in the presence of organic carbon (Hanesch et al., 2006), and it is not accompanied by a corresponding ferrimagnetic signal of this magnitude in the room-temperature data. This feature, and the marked χ increase and Hopkinson-like peak on cooling, are therefore interpreted mainly as thermal transformation products and are not used as evidence of the original magnetite content. The Curie temperatures near 550–580 °C nevertheless indicate that the neoformed (and any original) ferrimagnet is magnetite with a slight degree of non-stoichiometry or cation substitution (Dunlop and Özdemir, 1997; Liu et al., 2012). Evidence for the original mineralogy is instead drawn from the unheated samples: the low-temperature Verwey-like feature, room-temperature hysteresis, FORC and remanence parameters, and the XRD and Raman data (Figs. 4, 5, 7, 8, 9, 11 and 12; SFigs. 2, 3 and 6).

4.3 Concentration and coercivity of the magnetic minerals

The hysteresis loops showed a narrow central region, low coercivities Bc and Bcr, and a predominance of an easily magnetized component (Fig. 5 and SFig.3). Together, these characteristics indicate that the magnetic properties of the LVw are controlled mainly by low-coercivity ferrimagnetic minerals, such as magnetite and maghemite.

Stoichiometric magnetite has an Ms of ~92 A m^2 kg^{-1}, whereas maghemite has lower values, ~60–80 A m^2 kg^{-1} (Maher and Thompson, 1999; Peters and Dekkers, 2003). However, the Ms values (~ 76 × 10^{-3} A m^2 kg^{-1}) determined in soil samples are influenced by the concentration of the magnetic phases and, therefore, it is difficult to distinguish magnetite from maghemite directly in a mixed mineral assemblage. Thus, Ms values were used as indicators of variations in the concentration of magnetic minerals along the profile.

During the wetting season, the Ms distribution was more uniform in the upper horizons than during the drying season (Fig. 5 a). Despite the variations observed, the base of the profile remained characterized by lower values, reinforcing the interpretation that the greatest magnetic enhancement occurs in the surface horizons and is associated with pedogenic processes.

The local Ms maxima observed in the transition zones between horizons, particularly at depths of 15–20, 30–35, and 60–65 cm during the drying season, indicate localized increases in the concentration of the magnetic phases. These maxima may be related to Fe redistribution, to mineralogical and textural differences between horizons, or to the accumulation of pedogenesis products. The latter may produce nanoparticle aggregation and, consequently, increase the degree of magnetic interaction (Rebodos and Vikesland, 2010).

The S-ratio values (Fig. 5 f) indicated that low-coercivity phases, represented mainly by magnetite and maghemite, dominate the magnetic properties of the LVw. Although the S-ratio and HIRM are often used to estimate the relative contribution of high-coercivity minerals such as hematite and goethite, these parameters are influenced by both the concentration and the coercivity distribution of these phases. Al-for-Fe substitution, grain-size variations, and defects in the crystal structure can modify the coercivity of antiferromagnetic minerals and, consequently, affect the S-ratio and HIRM values (Liu et al., 2007). For this reason, the substitute L-ratio parameter was calculated for the samples of both periods.

Throughout most of the profile, the substitute L-ratio remained within a narrow range of values, close to 0.3 (Fig. 5 h), indicating relative uniformity in the coercivity distribution of the magnetically harder fraction. Under these conditions, HIRM variations can be interpreted mainly as changes in the relative concentration of high-coercivity minerals along the profile (Liu et al., 2007).

However, at the transition between the BA and Bw horizons, the substitute L-ratio showed the highest values of the sample series, specifically at depths of 40–45 and 60–65 cm during the DS and at 45–50 cm during the WS. At these depths, the variation in the substitute L-ratio may indicate changes in the coercivity distribution of the magnetically harder fraction. This change may be related to grain-size differences, isomorphic substitutions, crystal defects, provenance, or mixing between hematite populations with distinct magnetic properties (Liu et al., 2007).

The decomposition of the coercivity spectra from the IRM acquisition curves (Fig. 9 b) allowed two main magnetic populations to be distinguished. The Bh_{IRM} values of the first component (C1) were similar to those attributed to low-coercivity pedogenic magnetite, generally between 16 and 25 mT (Spassov et al., 2003; Maxbauer et al., 2016b, 2016c; Hyodo et al., 2020). In contrast, the higher Bh_{IRM} values of component C2 (mean ~230 mT; range ~90–550 mT) are compatible with partially oxidized pedogenic magnetite (~90–120 mT) (Maxbauer et al., 2016c) and hematite (> 200 mT) (Dunlop and Özdemir, 1997; Peters and Dekkers, 2003; Jordanova and Jordanova, 2016b; Maxbauer et al., 2016c; Hyodo et al., 2020). The greater logarithmic dispersion, DP, observed for the second component (C2) suggests a more heterogeneous coercivity population, possibly composed of particles of different sizes, degrees of substitution, or origins. This heterogeneity may reflect the coexistence of hematite inherited from the parent material and hematite formed or transformed during pedogenesis (Maxbauer et al., 2016b; Hyodo et al., 2020).

4.4 Magnetic grain size and domain state

In the Day diagram (Day et al., 1977; Dunlop, 2002a, b), the samples were concentrated predominantly in the pseudo-multi-domain (PSD) region (Fig. 6), which is commonly interpreted as a mixture of single-domain (SD) and multidomain (MD) particles or as vortex-state behavior, although the Day diagram is non-unique for natural mixtures (Roberts et al., 2018). The small

variation with depth indicates relative uniformity of the domain state along the profile. Even so, the shifts observed within the mixing region suggest subtle changes in the relative contribution of finer SD particles and coarser MD particles. However, the position of the values in the diagram is also influenced by mineral mixtures, magnetic interactions, and SP particles (Dunlop, 2002a, b).

The FORC diagrams (Fig. 7 and SFig. 4) showed coercivity maxima close to 8–10 mT, a vertical spread along the Bu axis at low Bc, and a narrow central ridge. These characteristics are compatible with a low-coercivity magnetite/maghemite assemblage in which vortex-state and thermally activated near-SP/SD particles coexist with non-interacting SD particles, the latter also indicated by Cisowski crossover values of ~0.5; magnetostatic interactions therefore appear to be weak. Similar behavior was reported by Almeida et al. (2015), who also pointed out that partial oxidation of the magnetite core with the formation of maghemite in the cortex can reduce the magnetization intensity and modify the coercivity distribution. Thus, the values of the FORC diagrams reinforce the interpretation of a fine, partially oxidized ferrimagnetic assemblage, although, by themselves, they do not determine the degree of stoichiometry of the minerals.

The relationship between the ratio χARM/SIRM and χfd% was used as a semi-quantitative indicator of magnetic grain size: χARM/SIRM is sensitive to stable SD particles and χfd% to SP particles near the blocking threshold (Maher, 1988; Dearing et al., 1997).

The distribution of the samples in the diagram (Fig. 13) indicates a strong contribution of SP particles to the susceptibility, in addition to the presence of particles distributed among the fields corresponding to coarse SSD, fine SSD, and grain-size mixtures. According to Dearing et al. (1997), the frequency-dependent response is associated mainly with SP particles with diameters smaller than approximately 0.03 μm and is more intense for particles located near the SP/SD threshold. The proportions indicated by the mixing lines of the diagram should, however, be interpreted semi-quantitatively, especially in natural samples that contain different minerals, magnetic interactions, and broad size distributions.

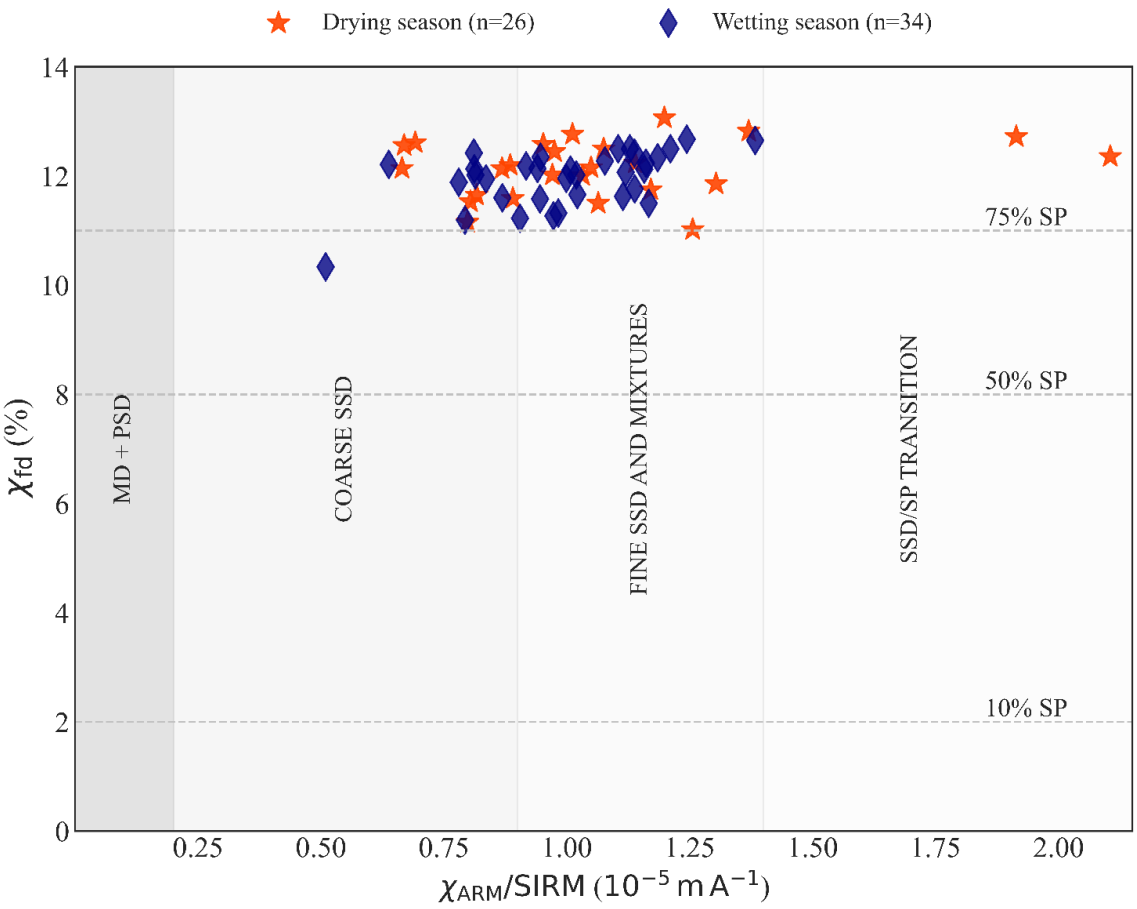


Figure 13. Semi-quantitative magnetic granulometry plot using χfd% versus χARM/SIRM (Dearing et al., 1997) for the DS and WS samples.

The decrease in χARM from the top to the base of the profile indicates that enrichment in fine ferrimagnetic particles occurs predominantly in the surface horizons. The strong positive correlations (~ 0.9) among χlf, χfd, and χARM (SFig. 8) show that the increase in magnetic susceptibility is associated with a higher concentration of fine particles, including SP and SD fractions. Together with the contrast between the surface horizons (χlf ~ 230 × 10^{-8} m^3 kg^{-1}; χfd ~ 12 %; χARM ~ 2000 × 10^{-8} m^3 kg^{-1}) and the parent material (χlf = 6.22 × 10^{-8} m^3 kg^{-1}; χfd = 3.95 %; χARM = 11.65 × 10^{-8} m^3 kg^{-1}), these relationships reinforce the contribution of pedogenesis to the magnetic enhancement of the LVw.

The weaker correlations (~ 0.4) of SIRM with χlf and χfd (SFig. 8) suggest that this parameter also responds to populations of larger particles. These populations may include coarser ferrimagnetic particles and higher-coercivity phases, possibly hematite. The magnetic assemblage of the LVw therefore comprises a fine pedogenic fraction, more abundant in the surface horizons, superimposed on contributions from coarser particles and antiferromagnetic minerals distributed throughout the profile.

4.5 Origin of the magnetic signature: Pedogenic versus lithogenic control

Lateritic soils are abundant in tropical regions (Tardy, 1997; Horbe and Costa, 1999; Reethu et al., 2023; Costa et al., 2026; Kadam et al., 2026) and, according to Preetz et al. (2017), the material on which *Latossolos* develop can determine the mechanism responsible for their magnetic enhancement. Because the parent rock strongly influences the mineralogical composition of these soils, different formation mechanisms of the ferrimagnetic phases can be observed. In soils developed from basic, intermediate, and ultrabasic rocks, magnetic enhancement may reflect a strong overprint of lithogenic inheritance, whereas in soils derived from slates and clays, the neoformation of ferrimagnetic minerals during pedogenesis may predominate (Jordanova, 2016; Preetz et al., 2017; Poggere et al., 2018).

Preetz et al. (2017) observed that, in profiles developed from weathered clays and slates, the neoformation of SP ferrimagnetic particles begins together with the lateritization process. This interpretation is compatible with the χfd value estimated for the parent rock in the present study. Such rocks, like slate, generally have low χlf values (< 10×10^{-8} m^3 kg^{-1}) (Maher and Taylor, 1988; Dearing et al., 1996b; Maher, 1998; Viana et al., 2016; Preetz et al., 2017), as was confirmed here (Table 1). Therefore, it seems unlikely that the magnetic enhancement observed in the surface horizons of the LVw (Fig. 2 a) was inherited directly from the rock on which the profile developed. Rather, the weathering of slate under tropical conditions appears to supply precursors in sufficient quantity for the pedogenic formation of ferrimagnetic particles of SP/SD size (Preetz et al., 2017).

The contrast is not limited to concentration. The slate is dominated by a high-coercivity phase (Bc ≈ 296 mT, Bcr ≈ 357 mT, S-ratio = 0.40; Table 1; SFig. 7 a, b), whereas the soil is dominated by low-coercivity ferrimagnets (Bc ≈ 5–10 mT; S-ratio = 0.93–1.00; Fig. 5 c, f), with higher χfd% (~12% versus ~4%) and χARM values two orders of magnitude higher (~825–2286 $\times 10^{-8}$ versus ~12×10^{-8} m^3 kg^{-1}). Residual accumulation of lithogenic minerals during weathering

could increase magnetic concentration, but it could not by itself shift the coercivity spectrum from hematite-dominated to fine-ferrimagnet-dominated. This mineral-magnetic contrast therefore requires the neoformation of fine ferrimagnetic particles during pedogenesis and constitutes the strongest line of evidence in this study.

The mineral-magnetic results reveal the coexistence of hematite and ferrimagnetic phases, consistent with the recurrent action of reduction, precipitation, and oxidation processes during pedogenesis. Therefore, under the conditions evaluated, it is possible to relate the Fe oxide minerals present in the LVw to the pedogenic model proposed by Dearing et al. (1996b) and later verified by Preetz et al. (2017) under tropical conditions.

4.6 A proposed mechanism for pedogenic magnetite formation

Having established that the enhancement is pedogenic rather than inherited, we now examine the coercivity of the fine ferrimagnetic fraction for evidence of a specific formation pathway and then propose a redox mechanism that could drive it; the limits of this inference are discussed in Section 4.7.

Because the maximum field applied during acquisition of the ARM curves was 100 mT, the decomposition of these spectra focused on the low-coercivity ferrimagnetic fraction. The MDF_{ARM} in both seasons were close to the value of approximately 15.1 mT (Fig. 10) found by Maher (1988) for fine, extracellularly precipitated magnetite. Moskowitz et al. (1989) also evaluated magnetites formed in an anaerobic environment and reported a median field of 18.9 mT for extracellular magnetite produced by the Fe-reducing bacterium GS-15, a value higher than the mean obtained for the LVw.

In Chinese paleosols, Egli (2004a) found MDF_{ARM} close to 18 mT and a logarithmic DP of approximately 0.30. Geiss et al. (2008), in turn, obtained values close to 20 mT and a DP of 0.32 in soils, associating them with pedogenic magnetite. Although these values are slightly higher than those observed in the LVw (Fig. 10), all remain within the range characteristic of low-coercivity ferrimagnetic phases. The results are also comparable to those of Jaqueto et al. (2021) for Cerrado soils, in which magnetic components attributed to detrital-extracellular and pedogenic contributions were identified. The mean MDF_{ARM} of approximately 18.4 mT reported by those authors was also higher than the values recorded in the present study.

Even so, the coercive properties of the LVw are compatible with fine pedogenic magnetite. The MDF_{ARM} values and χARM/SIRM ratios are also compatible, but not diagnostic of, extracellular (including bacterially mediated) magnetite: the same range overlaps with that of pedogenic and detrital magnetite (Egli, 2004a; Fig. 10), and no direct biogenic criteria, such as crystal morphology from TEM, microbiological data or incubation experiments, are available here. Microbial Fe (III) reduction is therefore treated as a proposed mechanism rather than a demonstrated origin.

In this context, the change in pH values observed between drying and wetting periods is compatible with seasonal changes, and changes in the oxidation state of the particles may occur. In addition, variations in the chemical environment can control the mobility and transformations of Fe (Özdemir et al., 1993; Cornell and Schwertmann, 2003; Ge et al., 2014; Almeida et al., 2015; Ahmed and Maher, 2018). However, because Eh and the Fe^{2+} and Fe^{3+} proportions were not determined, the observed variation in pH should be regarded as complementary evidence, and not as a direct measure of the intensity of redox processes.

Periodic reducing conditions may be favored by the high water supply during the wetting season. In central-western Brazil, under the same climate and lithology conditions as the present study, Macedo and Bryant (1989) found that the microenvironment around active or decomposing roots (rhizosphere) can remain under reducing conditions long enough to lower the redox potential of the soil. Under these conditions, the Fe^{3+} in the crystal structure of hematite can be used as an alternative electron acceptor during microbial respiration, and that the preferential reduction of hematite occurs rapidly, responding to current conditions of moisture, climate, and topographic position.

Even in predominantly oxidizing horizons, some pores may maintain temporarily anoxic microzones, especially in the transition between the wet period and the onset of soil drying. In the upper horizons, where organic matter availability is greater, biological activity is more intense and reducing bacteria can use Fe^{3+} as an alternative electron acceptor during their metabolism, producing dissolved Fe^{2+}. The coexistence of Fe^{2+} and Fe^{3+} in solution can favor the precipitation of SP/SSD-sized magnetite (Le Borgne, 1955; Maher, 1986; Maher and Taylor, 1988; Orgeira et al., 2011; Ahmed and Maher, 2018; Frankl et al., 2022).

With decreasing moisture and the progressive reoxygenation of the pores during the dry season, the previously mobilized Fe^{2+} can be reoxidized, creating favorable conditions for the extracellular precipitation of ferrimagnetic particles. Thus, the alternation between dissimilatory reduction of Fe^{3+}, promoted by specific groups of bacteria, and the subsequent reoxidation of the system could result in the formation of pedogenic magnetite (Lovley et al., 1987; Maher and Taylor, 1988, Maher, 1998; Ahmed and Maher, 2018; Frankl et al., 2022), a scenario consistent with, although not uniquely indicated by, the MDF values discussed above.

As the drying season advances and the oxygenation of the pore spaces increases, the newly formed magnetite particles are subject to different degrees of oxidation (Murad and Schwertmann, 1993; Orgeira et al., 2011). In certain environments, prolonged dry periods can promote partial or total oxidation of magnetite (Ahmed and Maher, 2018). Owing to the high surface-to-volume ratio of fine particles, maghemite can progressively become the predominant ferrimagnetic phase in different climatic contexts (Liu et al., 2004; Chen et al., 2005; Hu et al., 2015; Long et al., 2015; Gao et al., 2018).

However, the conditions evaluated in the present study combine a high seasonal water supply with good drainage capacity of the profile. In this scenario, reduction and oxidation cycles in the soil pores are modulated by the alternation between precipitation and evapotranspiration. After one or more cycles, the magnetite particles can again be subjected to reducing conditions similar to those that favored their initial formation. This new reduction cycle can promote the dissolution of the previously oxidized layer, resulting simultaneously in the formation of magnetite and the dissolution of maghemite during the soil redox cycles. As the profile develops, part of these grains may retain a maghemitized surface cortex and a core composed of magnetite. This structure can play an important role in preserving the grains, protecting their inner core against further transformation or dissolution (Maher, 1988, 1998; Orgeira et al., 2011; Ahmed and Maher, 2018), according to the model proposed in Fig. 14 (This figure is exclusive to the journal being considered for publication and will not be shared beforehand).

Under the continued action of this mechanism, the magnetic enhancement of the soil tends to be controlled by the presence of magnetite (Ahmed and Maher, 2018; Zhang et al., 2020; Gao et al., 2022). Because the oxidation process acts in the formation of maghemite, the high $\chi fd\%$ values recorded in both sampling periods can be attributed to the high proportion of SP particles

of magnetite and maghemite. These particles can occur either as extracellular precipitates resulting from bacterial reduction during pedogenesis (Zhang et al., 2020) or as products of the partial oxidation of the initially formed magnetite (Ge et al., 2014; Almeida et al., 2015).

Taken together, the results presented demonstrate the difference between the magnetic signature of the soil profile and that of the parent material. Therefore, the hypothesis that the magnetic enhancement of this soil results from pedogenic processes is supported by the data, and its expression is consistent with the cumulative effect of repeated drying and wetting cycles. These cycles may favor Fe mobilization, the neoformation of SP/SD ferrimagnetic particles, and their subsequent partial oxidation, resulting in a set of magnetic minerals composed mainly of magnetite and maghemite. In this process, dissimilatory microbial reduction of Fe^{3+} represents a plausible mechanism for the formation of pedogenic magnetite, although this pathway was not directly demonstrated in the present study.

4.7 Limited seasonal response: An integrated pedogenic memory

The most robust seasonal result of this study is the absence of large magnetic differences between the DS and WS profiles, despite the contrasting hydrological conditions of the two campaigns (Section 2.1; Fig. 2a). χlf, χfd%, Bc, S-ratio, χARM and MDF_{ARM} component show similar depth patterns and overlapping ranges in both seasons (Figs. 3, 5, 8 and 10). Thus, we interpret this as evidence that the magnetic signature of this soil is an integrated pedogenic memory of repeated wetting–drying cycles rather than a rapidly reversible mineralogical response to a single season. If one wet season produces, dissolves or oxidizes only a small quantity of fine ferrimagnetic particles relative to the stock accumulated over the history of the soil, seasonal changes are expected to be small compared with the depth-related variation and, especially, with the ~30-fold contrast between the upper horizons and the parent slate. This behavior agrees with the relative stability of magnetic assemblages in mature, intensely weathered soils (Maxbauer et al., 2016a) and does not exclude microscale redox reactions, which may be transient or produce partially compensating effects (Stumm and Sulzberger, 1992). It implies that, in well-drained tropical soils, magnetic properties are better suited as indicators of long-term pedogenic redox history than of short-term seasonal dynamics.

Three features of the study limit inference on seasonal processes. First, this is a profile-scale case study: one profile was sampled on two occasions, so the depth intervals are not

independent replicates of drying- and wetting-season conditions, and the results should not be generalized to Cerrado *Latossolos* without spatial replication. Second, the two campaigns captured two temporal states of the profile rather than the same soil volumes followed longitudinally; differences between campaigns therefore cannot be equated with in situ transformation of a single mineral population within one seasonal cycle. Third, all samples were air-dried before analysis, which may have partially oxidized the finest magnetite and removed transient differences in field moisture and redox state; in addition, Eh, soil O_2, dissolved Fe^{2+}/Fe^{3+} and microbial activity were not measured. Resolving whether a single wetting season measurably modifies the ferrimagnetic assemblage will require replicated profiles, repeated sampling of the same soil volumes, samples preserved under anoxic conditions, *in situ* redox monitoring and microbiological analyses.

5. Conclusions

The difference in magnetic signature between the parent material and the surface horizons (χlf up to ~233×10^{-8} m^3 kg^{-1}, more than 30 times that of the parent slate) indicates that the magnetic enhancement of the *Latossolo Vermelho* (Oxisol/Ferralsol) is predominantly pedogenic. We propose that dissimilatory microbial reduction of Fe^{3+} is a plausible, but not demonstrated, pathway for the formation of pedogenic magnetite. Extracellular precipitation could occur in anoxic microzones established during the wetting period and temporarily maintained at the onset of drying, in which reducing bacteria use Fe^{3+} as an alternative electron acceptor and release Fe^{2+}. As the pores are reoxygenated during drying, these particles could be oxidized to maghemite-hematite.

In this sense, the coexistence of magnetite, maghemite and hematite, associated with evidence of non-stoichiometry and oxidation of magnetite, is consistent with a model in which recurrent wetting and drying cycles favor Fe mobilization, the neoformation of SP/SSD ferrimagnetic particles, and their transformation by oxidation, producing a mineral assemblage dominated by vortex-state (PSD) and non-interacting SD particles. Despite contrasting hydrological conditions, differences between the drying and wetting seasons profiles were subtle; the magnetic signature therefore behaves as an integrated pedogenic memory of repeated wetting–drying cycles rather than a rapidly reversible response to a single season.

Because this is a profile-scale case study, sampled on two occasions, these conclusions should be tested with spatially replicated profiles and repeated sampling of the same soil volumes. Although the organic matter, carbon, and hydrogen contents indicate the availability of an organic substrate potentially favorable to microbial metabolism, the factors controlling the operation of this pathway must be confirmed by specific geochemical and microbiological analyses.

In addition, future environmental magnetism studies in the Brazilian Cerrado should verify the presence of charcoal in soil profiles, since wildfire events are recurrent, and this is another pathway of pedogenic formation of ferrimagnetic particles to be considered in this climatic context. Lastly, should explore other Cerrado environments and include other soil classes with different histories of use and occupation, to expand the applicability of magnetic properties as pedoenvironmental indicators.

Declaration of competing interest

The authors declare that they have no known competing financial interests or personal relationships that could have appeared to influence the work reported in this paper.

Acknowledgements and funding

This study acknowledges the Institute of Astronomy, Geophysics and Atmospheric Sciences of the University of São Paulo (IAG-USP) for granting the *grant* that enabled the development of the magnetic methods, all carried out at the Paleomagnetism Laboratory (IAG-USP). To the Research Support Foundation of the Federal District (FAP-DF), for financing the project "Magnetic susceptibility and soil quality in burned areas in conservation units and parks of the Federal District", number 00193-00001214/2021-80. This study was financed in part by the Coordenação de Aperfeiçoamento de Pessoal de Nível Superior - Brasil (CAPES) - Finance Code 001, through the doctoral scholarship granted to the first author. We thank illustrator Alessandra Caiafa for her contribution to the development of the graphical abstract, based on the concept and sketch prepared by the first author.

References

Ahmed, I. A., Maher, B. A., 2018. Identification and paleoclimatic significance of magnetite nanoparticles in soils. Proceedings of the National Academy of Sciences, 115, 1736-1741. https://doi.org/10.1073/pnas.1719186115.

Almeida, T. P., Muxworthy, A. R., Kasama, T., Williams, W., Damsgaard, C., Frandsen, C., Pennycook, T. J., Dunin-Borkowski, R. E., 2015. Effect of maghemization on the magnetic properties of nonstoichiometric pseudo-single-domain magnetite particles. Geochemistry, Geophysics, Geosystems, 16, 2969-2979.**https://doi.org/10.1002/ 2015GC005858**.

Alvares, C.A., Stape, J.L., Sentelhas, P.C., Gonçalves, J.L.M., Sparovek, G., 2013. Köppen's climate classification map for Brazil. Meteorologische Zeitschrift 22, 711–728. https://doi.org/10.1127/0941-2948/2013/0507.

Balsam, W. L., Ellwood, B. B., Ji, J., Williams, E. R., Long, X., & El Hassani, A., 2011. Magnetic susceptibility as a proxy for rainfall: worldwide data from tropical and temperate climate. Quaternary Science Reviews, 30, 2732-2744. https://doi.org/10.1016/ j.quascirev.2011.06.002.

Barbosa, I. O., Lacerda, M. P. C., Bilich, M. R., 2009. Relações pedomorfogeológicas nas chapadas elevadas do Distrito Federal. R. Brasi. Ci. Solo, 33, 1373-1383. https://doi.org /10.1590/S0100-06832009000500029.

Barbosa, J.Z., Poggere, G., Silva, S.H.G., Mancini, M., Motta, A.C.V., Marques, J.J.G.S.M., Curi, N., 2021. National-scale spatial variations of soil magnetic susceptibility in Brazil. J. S. Am. Earth Sci. 108, 103191. https://doi.org/10.1016/j.jsames.2021.103191.

Barrón, V., Torrent, J., 2002. Evidence for a simple pathway to maghemite in Earth and Mars soils. Geochim. Cosmochim. Acta 66, 2801–2806. https://doi.org/10.1016/S0016-7037(02)00876-1.

Bloemendal, J., King, J.W., Hall, F.R., Doh, S.J., 1992. Rock magnetism of Late Neogene and Pleistocene deep-sea sediments: relationship to sediment source, diagenetic processes, and sediment lithology. J. Geophys. Res. 97, 4361–4375. http://dx.doi.org/ 10.1029/91JB03068.

Camêlo, D.D.L., Ker, J.C., Fontes, M.P.F., Costa, A.C.S., Corrêa, M.M., Leopold, M., 2018. Mineralogy, magnetic susceptibility and geochemistry of Fe-rich Oxisols developed from several parent materials. Sci. Agric. 75, 410–419. https://doi.org/10.1590/1678-992X-2017-0087.

Camêlo, D.L.; Ker, J.C.; Fontes, M.P.F.; Corrêa, M.M.; Costa, A.C.S.; Melo, V.F. 2017. Pedogenic iron oxides in iron-rich Oxisols developed from mafic rocks. Rev Bras Cienc Solo 41: e0160379. https://doi.org/10.1590/18069657rbcs20160379.

Campos, J.E.G., Dardenne, M.A., Freitas-Silva, F.H., Martins-Ferreira, M.A.C., 2013. Geologia do Grupo Paranoá na porção externa da Faixa Brasília. Brazilian Journal of Geology 43 (3), 461–476. doi: 10.5327/Z2317-48892013000300004.

Campos, P. M. 2009. Influência físico-hídrica nos atributos diagnósticos em Latossolos do Distrito Federal. M. Sc Diss. Universidade de Brasília, Brasília-DF, Brazil. 110 p.

Campos, P. M., Lacerda, M. P. C., Silva, C. L. D., Sá, M. A. C. D., Sousa, D. M. G. D. 2010. Drenagem interna como fator de diferenciação de Latossolos do Distrito Federal. Pesq. agropec. bras., 45(3),306-314. https://doi.org/10.1590/S0100-204X2010000300011.

Chen, T., Xu, H., Xie, Q., Chen, J., Ji, J., Lu, H., 2005. Characteristics and genesis of maghemite in Chinese loess and paleosols: mechanism for magnetic susceptibility enhancement in paleosols. Earth and Planetary Science Letters, 240, 790-802. https://doi.org/10.1016/j.epsl.2005.09.026.

Churchman, G.J., Lowe, D.J., 2012. Alteration, formation, and occurrence of minerals in soils. In: Huang, P.M., Li, Y., Sumner, M.E. (Eds.), Handbook of Soil Sciences: Properties and Processes, second ed. CRC Press, Taylor & Francis, Boca Raton, Florida, pp. 20.1–20.72.

Cisowski, S., 1981. Interacting vs non-interacting single domain behavior in natural and synthetic samples, Phys. Earth Planet. In., 26, 56–62. https://doi.org/10.1016/0031-9201(81)90097-2.

Cornell, R. M., Schwertmann, U., 2003. The Iron Oxides: Structure, Properties, Reactions, Occurrences and Uses, second ed. Wiley, New York.

Costa, M. L. D., Abreu, D. S., Santos, P. H. C. D., Leite, A. S., 2026. Formation and degradation of immature laterites in response to paleoclimatic changes in the eastern Amazon. Brazilian Journal of Geology, 56, e20250022. https://doi.org/10.1590/2317-4889e20250022.

Day, R., Fuller, M., Schmidt, V. A., 1977. Hysteresis properties of titanomagnetites: grain-size and compositional dependence. Physics of the Earth and planetary interiors, 13, 260-267. https://doi.org/10.1016/0031-9201(77)90108-X.

de Boer, C. B., Dekkers, M. J., and van Hoof, T. A., 2001. Rock-magnetic properties of TRM carrying baked and molten rocks straddling burnt coal seams. Physics of the Earth and Planetary Interiors, 126, 93-108. doi:10.1016/S0031-9201(01)00246-1.

Dearing, J. A., Bird, P. M., Dann, R. J. L., Benjamin, S. F., 1997. Secondary ferrimagnetic minerals in Welsh soils: a comparison of mineral magnetic detection methods and implications for mineral formation, Geophysical Journal International, 130, 727–736, https://doi.org/10.1111/j.1365-246X.1997.tb01867.x.

Dearing, J. A., Dann, R. J. L., Hay, K., Lees, J. A., Loveland, P. J., Maher, B. A., & O'Grady, K., 1996a. Frequency-dependent susceptibility measurements of environmental materials. Geophysical Journal International, 124, 228-240. https://doi.org/10.1111/j.1365-246X.1996.tb06366.x.

Dearing, J.A., Hay, K.L., Baban, S.M.J., Huddleston, A.S., Wellington, E.M.H., Loveland, P.J., 1996b. Magnetic susceptibility of soil: an evaluation of conflicting theories using a national data set. Geophys. J. Int. 127, 728–734. https://doi.org/10.1111/j.1365-246X.1996.tb04051.x.

Dunlop, D. J., 2002a. Theory and application of the Day plot (M_{rs}/M_s versus H_{cr}/H_c), 1. Theoretical curves and tests using titanomagnetite data, J. Geophys. Res., 107, **https://doi.org/10.1029/2001JB000486**.

Dunlop, D. J., 2002b. Theory and application of the Day plot (M_{rs}/M_s versus H_{cr}/H_c) 2. Application to data for rocks, sediments, and soils, J. Geophys. Res., 107. **https://doi.org/10.1029/2001JB000487**.

Dunlop, D.J., Özdemir, Ö., 1997. Rock Magnetism. Cambridge University Press, Cambridge doi:10.1017/CBO9780511612794.

Egli, R., 2003. Analysis of the field dependence of remanent magnetization curves. J. Geophys. Res. 108, 1–25. http://dx.doi.org/10.1029/2002JB002023.

Egli, R., 2004a. Characterization of individual rock magnetic components by analysis of remanence curves, 1. Unmixing natural sediments. Stud. Geophys. Geod. 48, 391–446. http://dx.doi.org/10.1023/B:SGEG.0000020839.45304.6d.

Egli, R., 2004b. Characterization of individual rock magnetic components by analysis of remanence curves. 2. Fundamental properties of coercivity distributions. Phys. Chem. Earth 29, 851–867. http://dx.doi.org/10.1016/j.pce.2004.04.001.

Egli, R., Chen, A.P., Winklhofer, M., Kodama, K.P., Horng, C.-S., 2010. Detection of noninteracting single domain particles using first-order reversal curve diagrams. Geochemistry, Geophysics, Geosystems 11, Q01Z11. https://doi.org/10.1029/2009GC002916.

Eswaran, H., Kimble, J., Cook, T., & Beinroth, F. H., 1992. Soil diversity in the tropics: implications for agricultural development. Myths and Science of Soils of the Tropics, 29, 1-16. **https://doi.org/10.2136/sssaspecpub29.c1**.

Fontes, M.P.F.; Oliveira, T.S.; Costa, L.M.; Campos, A.A.G. 2000. Magnetic separation and evaluation of magnetization of Brazilian soils from different parent materials. Geoderma 96: 81-99. 10.1016/S0016-7061(00)00005-7.

Frankl, A. L., Maxbauer, D. P., Savina, M. E., 2022. Linkages between soil organic matter and magnetic mineral formation in agricultural fields in southeastern Minnesota, USA. Geoderma, 406, 115466. https://doi.org/10.1016/j.geoderma.2021.115466.

Gao, P., Nie, J., Breecker, D. O., Gallagher, T., Serach, L., & Alonso-Zarza, A. M., 2022. Similar magnetic enhancement mechanisms between Chinese loess and alluvial sediments from the Teruel Basin, NE Spain, and paleoclimate implications. Geophysical Research Letters, 49, e2021GL096977. **https://doi.org/10.1029/ 2021GL096977**.

Gao, X., Hao, Q., Oldfield, F., Bloemendal, J., Deng, C., Wang, L., Song, Y., Ge, J., Bing, X., Li, F., Han, L., Fu, Y., Guo, Z., 2019. New high-temperature dependence of magnetic susceptibility-based climofunction for quantifying paleoprecipitation from Chinese loess. Geochemistry, Geophysics, Geosystems, 20, 4273-4291. https://doi.org/10.1029/2019GC008401.

Gao, X., Hao, Q., Wang, L., Oldfield, F., Bloemendal, J., Deng, C., Song, Y., Ge, J., Wu, H., Xu, B., Li, F., Han, L., Fu, Y., Guo, Z., 2018. The different climatic response of pedogenic hematite and ferrimagnetic minerals: Evidence from particle-sized modern soils over the Chinese Loess Plateau. Quaternary Science Reviews, 179, 69-86. https://doi.org /10.1016/j.quascirev.2017.11.011.

Ge, K., Williams,W., Liu, Q., Yu, Y., 2014. Effects of the core-shell structure on themagentic properties of partially oxidized magentite grains: experimental and micromagnetic investigations. Geochem. Geophys. Geosyst. 15, 2021–2038. http://dx.doi.org/10. 1002/2014GC005265.

Geiss, C.E., Egli, R., Zanner, C.W., 2008. Direct estimates of pedogenicmagnetite as a tool to reconstruct past climates from buried soils. J. Geophys. Res. 113, B11102. http://dx.doi.org/10.1029/2008JB005669.

Golfari, L., 1978. Forestry development and research. Brazil. Zoning for reforestation in Brazil and trials with tropical Eucalyptus and pines in central region.

Han, J.M., Lu, H.Y., Wu, N.Q., Gui, Z.T., 1996. The magnetic susceptibility of modern soils in China and its use for paleoclimate reconstruction. Stud Geophys Geod 40, 262–275. https://doi.org/10.1007/BF02300742.

Hanesch, M., 2009. Raman spectroscopy of iron oxides and oxy(hydroxides) at lower laser power and possible application in environmental magnetic studies. Geophysical Journal International 177, 941–948. https://doi.org/10.1111/j.1365-246X.2009. 04122.x.

Hanesch, M., Petersen, N., 1999. Magnetic properties of a recent parabrown-earth from Southern Germany. Earth and Planetary Science Letters, 169, 85-97. https://doi.org/ 10.1016/S0012-821X(99)00076-X.

Hanesch, M., Stanjek, H., Petersen, N., 2006. Thermomagnetic measurements of soil iron minerals: the role of organic carbon. Geophysical Journal International 165, 53–61. https://doi.org/10.1111/j.1365-246X.2006.02933.x.

Heslop, D., Roberts, A. P., Oda, H., Zhao, X., Harrison, R. J., Muxworthy, A. R., Hu, P.X., Sato, T., 2020. An automatic model selection-based machine learning framework to estimate FORC distributions. Journal of Geophysical Research: Solid Earth, 125, e2020JB020418. **https://doi.org/10.1029/2020JB020418**.

Hyodo, M., Sano, T., Matsumoto, M., Seto, Y., Bradák, B., Suzuki, K., Fukuda, J., Shi, M., Yang, T., 2020. Nanosized authigenic magnetite and hematite particles in mature-paleosol phyllosilicates: new evidence for a magnetic enhancement mechanism in loess sequences of China. J. Geophys. Res. Solid Earth. 125, 1–25. https://doi.org /10.1029/2019JB018705.

Horbe, A. M. C., Costa, M. L., 1999. Relações genéticas entre Latossolos e crostas lateríticas aluminosas e alumino-ferruginosas na região de Paragominas, Pará. Brazilian Journal of Geology, 29, 497-504.

Hu, P., Heslop, D., Viscarra Rossel, R. A., Roberts, A. P., and Zhao, X., 2020. Continental-scale magnetic properties of surficial Australian soils. Earth Sci. Rev. https://doi.org/ 10.1016/j.earscirev.2019.103028.

Hu, P., Liu, Q., Heslop, D., Roberts, A.P., Jin, C., 2015. Soil moisture balance and magnetic enhancement in loess–paleosol sequences from the Tibetan Plateau and Chinese Loess Plateau. Earth Planet. Sci. Lett. 409, 120–132. http://dx.doi.org /10.1016/ j.epsl2014.10.035.

IUSS Working Group WRB. 2022. World Reference Base for Soil Resources. International soil classification system for naming soils and creating legends for soil maps, fourth ed. International Union of Soil Sciences (IUSS), Vienna, Austria.

Jackson, M. L., 1969. Soil chemical analysis. Advanced course, second ed. Dept. Soil Science, University of Wisconsin, Madison, WI, USA.

Jaqueto, P., Trindade, R. I., Feinberg, J. M., Carmo, J., Novello, V. F., Stríkis, N. M., Cruz, F. W., Shimizu, M.H., Karmann, I., 2021. Magnetic mineralogy of speleothems from tropical-subtropical sites of South America. Frontiers in Earth Science, 9, 634482. https://doi.org/10.3389/feart.2021.634482.

Jaqueto, P., Trindade, R. I., Hartmann, G. A., Novello, V. F., Cruz, F. W., Karmann, I., Strauss, B. E., Feinberg, J. M.,2016. Linking speleothem and soil magnetism in the Pau d'Alho cave (central South America). Journal of Geophysical Research: Solid Earth, 121, 7024-7039. https://doi.org/10.1002/2016JB013541.

Jordanova, D., Jordanova, N., 2016a. Thermomagnetic behavior of magnetic susceptibility—Heating rate and sample size effects. Frontiers in Earth Science, 3. https://doi.org/10.3389/feart.2015.00090.

Jordanova, N., 2016. Soil Magnetism: Applications in Pedology, Environmental Science and Agriculture, first ed. Academic Press (Elsevier).

Jordanova, N., Jordanova, D., 2016b. Rock-magnetic and geochemical characteristics of relict Vertisols—Signs of past climate and recent pedogenic development. Geophysical Journal International, 205, 1437-1454. https://doi.org/10.1093/gji/ggw067.

Kadam, N., Lascu, I., Wagner, C., 2026. Magnetic mineral characterization of laterites from peninsular India: Inferences on their genesis and utility in paleomagnetic and paleoenvironmental studies. Journal of Geophysical Research: Solid Earth, 131, e2025JB033425. **https://doi.org/10.1029/2025JB033425**.

Kämpf, N., Curi, N., & Marques, J. J., 2009. Intemperismo e ocorrência de minerais no ambiente do solo. in: Melo, V. F., Alleoni, L. R. F. (Eds.), Química e mineralogia do solo parte I - conceitos básicos. SBCS, Viçosa, pp. 333–379.

Kämpf, N., Curi, N., 2000. Óxidos de ferro: Indicadores de ambientes pedogênicos e geoquímicos. Tópicos Cienc Solo, 1, pp. 107-138.

Ker, J. C., 1997. Latossolos do Brasil: uma revisão. Revista Geonomos, 5.

Ker, J. C., Curi, N., Schaefer, C. E. G. R., Vidal-Torrado, P. 2012. Pedologia: Fundamentos, first ed. SBCS, Viçosa

Krishnamurti, D., 1958. The Raman spectrum of quartz and its interpretation. In: Proceedings of the Indian Academy of Sciences – Section A. Springer India, New Delhi, pp. 276–291.

Le Borgne, E., 1955. Susceptbilite magnetique anoramle du sol superficiel. Ann. Geophys., 11, 399-419.

Lepre, C. J., 2026. Origins of soil magnetism in alluvial-lacustrine environments: Insights from Early Pleistocene paleosols of the northern Kenyan rift. Catena, 267, 109996. https://doi.org/10.1016/j.catena.2026.109996.

Lepre, C., 2023. Identifying temperature and moisture controls on Fe oxide origins. Geophysical Research Letters, 50, e2023GL102761. **https://doi.org/10.1029/2023GL 102761**.

Liu, Q., Banerjee, S. K., Jackson, M. J., Deng, C., Pan, Y., Rixiang, Z., 2004. New insights into partial oxidation model of magnetites and thermal alteration of magnetic mineralogy of the Chinese loess in air. Geophysical Journal International, 158, 506-514. https:// doi.org/10.1111/j.1365-246X.2004.02348.x.

Liu, Q., Deng, C., Yu, Y., Torrent, J., Jackson, M. J., Banerjee, S. K., Zhu, R., 2005. Temperature dependence of magnetic susceptibility in an argon environment: implications for pedogenesis of Chinese loess/palaeosols. Geophysical Journal International, 161, 102-112. https://doi.org/10.1111/j.1365-246X.2005.02564.x.

Liu, Q., Roberts, A. P., Larrasoaña, J. C., Banerjee, S. K., Guyodo, Y., Tauxe, L., Oldfield, F., 2012. Environmental magnetism: Principles and applications, Rev. Geophys., 50, RG4002. **https://doi.org/10.1029/2012RG000393**.

Liu, Q., Roberts, A.P., Torrent, J., Horng, C.-S., Larrasoaña, J.C., 2007. What do the HIRM and S-ratio really measure in environmental magnetism? Geochemistry, Geophysics, Geosystems 8, Q09011. https://doi.org/10.1029/2007GC001717.

Long, X., Ji, J., Balsam, W., Barrón, V., Torrent, J., 2015. Grain growth and transformation of pedogenic magnetic particles in red Ferralsols. Geophysical Research Letters, 42(14), 5762-5770. **https://doi.org/10.1002/2015GL064678**.

Lovley, D.R., Stolz, J.F., Nord. G.L., Phillips, E.J.P., 1987. Anaerobic production of magnetite by a dissimilatory iron reducing microorganism. Nature 330, 252-254. https:// doi.org/10.1038/330252a0.

Macedo, J., Bryant, R. B., 1989. Preferential microbial reduction of hematite over goethite in a Brazilian Oxisol. Soil Science Society of America Journal, 53, 1114-1118. **https://doi.org/10.2136/sssaj1989.03615995005300040022x**.

Maher, B. A., 1986. Characterisation of soils by mineral magnetic measurements. Physics of the Earth and planetary interiors, 42, 76-92. https://doi.org/10.1016/S0031-9201(86) 80010-3.

Maher, B. A., 1988. Magnetic properties of some synthetic sub-micron magnetites. Geophysical Journal International, 94, 83-96. https://doi.org/10.1111/j.1365-246X.1988.tb03 429.x.

Maher, B.A., 1998. Magnetic properties of modern soils and Quaternary loessic paleosols: paleoclimatic implications. Palaeogeogr. Palaeoclimatol. Palaeoecol. 137, 25–54. http://dx.doi.org/10.1016/S0031-0182(97)00103-X.

Maher, B.A., 2011. The magnetic properties of Quaternary aeolian dusts and sediments, and their palaeoclimatic significance. Aeolian Res. 3, 87–144. doi:10.1016/j.aeolia.2011.01.005.

Maher, B.A., Alekseev, A., Alekseeva, T., 2003. Magnetic mineralogy of soils across the Russian Steppe: climatic dependence of pedogenic magnetite formation. Palaeogeography Palaeoclimatology Palaeoecology 201, 321–341. https://doi.org/10.1016/S0031-0182(03)00618-7.

Maher, B.A., Taylor, R.M., 1988. Formation of ultrafine-grained magnetite in soils. Nature 336, 368–370. https://doi.org/10.1038/336368a0.

Maher, B.A., Thompson, R.,1992. Paleoclimatic significance of the mineral magnetic record of the Chinese loess and paleosols. Quat. Res. 37, 155e170. doi: 10.1016/0033-5894 (92)90079-X.

Maher, B.A., Thompson, R., 1999. Paleomonsoons. I. The paleoclimatic record of the Chinese loess and palaeosols. In: Maher, B.A., Thompson, R. (Eds.), Quaternary Climates, Environments and Magnetism. Cambridge University Press, pp. 81–125.

Maher, B.A., Thompson, R., 1995. Paleorainfall reconstructions from pedogenic magnetic susceptibility variations in the Chinese loess and paleosols. Quat. Res. 44, 383e391. doi: 10.1006/qres.1995.1083.

Maher, B.A., Thompson, R., Zhou, L.P., 1994. Spatial and temporal reconstructions of changes in the Asian palaeomonsoon – a new mineral magnetic approach. Earth and Planetary Science Letters 125, 461–471. https://doi.org/10.1016/0012-821X(94)90232-1.

Mallett, T., Lise-Pronovost, A., Jaqueto, P., Black, J. R., Carmo, J., Trindade, R. I., Sniderman, J. M. K., Matley, K. A. and Woodhead, J. D., 2025. Environmental magnetism of late Holocene stalagmites from semi-arid karst in southern Australia. Quaternary Science Reviews, 356, 109290. https://doi.org/10.1016/j.quascirev.2025.109290

Marshall, C.P., Stockdale, G., Carr, C.A., 2025. Raman spectroscopy of geological varieties of hematite of varying crystallinity and morphology. Journal of Raman Spectroscopy, 56, 590–597. https://doi.org/10.1002/jrs.6811.

Maxbauer, D. P., Feinberg, J. M., Fox, D. L., 2016a. Magnetic mineral assemblages in soils and paleosols as the basis for paleoprecipitation proxies: A review of magnetic methods and challenges. Earth-Science Reviews, 155, 28-48. http://dx.doi.org/10.1016/j.earscirev.2016.01.014.

Maxbauer, D. P., Feinberg, J. M., Fox, D. L., 2016b. MAX UnMix: A web application for unmixing magnetic coercivity distributions. Computers & Geosciences, 95, 140-145. https://doi.org/10.1016/j.cageo.2016.07.009.

Maxbauer, D. P., Feinberg, J. M., Fox, D. L., Clyde, W. C., 2016c. Magnetic minerals as recorders of weathering, diagenesis, and paleoclimate: A core–outcrop comparison of Paleocene–

Eocene paleosols in the Bighorn Basin, WY, USA. Earth and Planetary Science Letters, 452, 15-26. http://dx.doi.org/10.1016/j.epsl.2016.07.029.

Mekaru, T., Uehara, G., 1972. Anion adsorption in ferruginous tropical soils. Soil Science Society of America Journal 36, 296–300.

Moskowitz, B. M., Frankel, R. B., Bazylinski, D. A., Jannasch, H. W., Lovley, D. R., 1989. A comparison of magnetite particles produced anaerobically by magnetotactic and dissimilatory iron-reducing bacteria. Geophysical Research Letters, 16, 665-668. **https://doi.org/10.1029/GL016i007p00665**.

Murad, E., Schwertmann, U., 1993. Temporal stability of a fine-grained magnetite. Clays and clay minerals, 41, 111-113. https://doi.org/10.1346/CCMN.1993.0410112.

Muxworthy, A. R., Turney, J. N., Qi, L., Baker, E. B., Perkins, J. R., Abdulkarim, M. A., 2023. Interpreting high-temperature magnetic susceptibility data of natural systems. Frontiers in Earth Science, 11, 1171200. https://doi.org/10.3389/feart.2023.1171200.

Namduri, H., Nasrazadani, S., 2008. Quantitative analysis of iron oxides using Fourier transform infrared spectrophotometry. Corrosion Science 50, 2493–2497. https://doi.org /10.1016/j.corsci.2008.06.034.

Oh, S.J., Cook, D.C., Townsend, H.E., 1998. Characterization of iron-oxides commonly formed as corrosion products on steel. Hyperfine Interactions 112, 59–65. https://doi.org /10.1023/A:1011076308501.

Opriș, O., Stegarescu, A., Lung, I., Porav, A. S., Kacso, I., Borodi, G., Leostean, C., Panã, O., Soran, M. L., 2025. Preparation and Characterization of Materials Based on Graphene Oxide Functionalized with Fe, Mn, Ni, and Cu Oxides and Their Testing for the Removal of Water Pollutants. Materials, 18, 2735. https://doi.org/10.3390/ma1 8122735.

Orgeira, M.J., Egli, R., Compagnucci, R.H., 2011. A Quantitative Model of Magnetic Enhancement in Loessic Soils. In: Petrovský, E., Ivers, D., Harinarayana, T., Herrero-Bervera, E. (eds) The Earth's Magnetic Interior. IAGA Special Sopron Book Series, 1. Springer, Dordrecht. https://doi.org/10.1007/978-94-007-0323-0_25.

Özdemir, Ö., Dunlop, D. J.,Moskowitz, B. M., 1993. The effect of oxidation on the Verwey transition in magnetite. Geophysical Research Letters, 20, 1671-1674. **https:// doi.org/10.1029/93GL01483**.

Özdemir, Ö., Dunlop, D.J., Berquó, T.S., 2008. Morin transition in hematite: size dependence and thermal hysteresis. Geochemistry, Geophysics, Geosystems 9, Q10Z01. https:// doi.org/10.1029/2008GC002110.

Peters, C., Dekkers, M. J., 2003. Selected room temperature magnetic parameters as a function of mineralogy, concentration and grain size. Physics and Chemistry of the Earth, Parts A/B/C, 28, 659-667. https://doi.org/10.1016/S1474-7065(03)00120-7.

Poggere, G. C., Inda, A. V., Barron, V., Kämpf, N., de Brito, A. D. B., Barbosa, J. Z., Curi, N., 2018. Maghemite quantification and magnetic signature of Brazilian soils with contrasting parent materials. Applied Clay Science, 161, 385-394. https://doi.org/ 10.1016/j.clay.2018.05.014.

Preetz, H., Igel, J., Hannam, J. A., & Stadler, S., 2017. Relationship between magnetic properties and reddening of tropical soils as indicators of weathering. Geoderma, 303, 143-149. http://dx.doi.org/10.1016/j.geoderma.2017.05.007.

Ramos, P.V., Dalmolin, R.S.D., Marques Júnior, J., Siqueira, D.S., Almeida, J.A.D., Moura-Bueno, J.M., 2017. Magnetic susceptibility of soil to differentiate soil environments in southern Brazil. Rev. Bras. Cienc. Solo. 41. https://doi.org/10.1590/18069657rbcs2016 0189.

Rebodos, R. L., Vikesland, P. J. 2010. Effects of oxidation on the magnetization of nanoparticulate magnetite. Langmuir, 26, 16745-16753. https://doi.org/10.1021/la10 2461z.

Reethu, M., Sandeep, K., Sebastian, J. G., Warrier, A. K., Aravind, G. H., Rafaz, A. K., Jose, J., Akshay, R., Suhaiba, V., 2023. Mineral magnetic properties of ultisol profiles from tropical southern India. Geosci J 27, 581–598. https://doi.org/10.1007/s12303-023-0017-6.

Ritchie, G. S. P.,Dolling, P. J., 1985. The role of organic matter in soil acidification. Australian Journal of Soil Research, 23, 569-576. https://doi.org/10.1071/SR9850569.

Roberts, A. P., Pike, C. R., Verosub, K. L., 2000. First-order reversal curve diagrams: A new tool for characterizing the magnetic properties of natural samples. Journal of Geophysical Research: Solid Earth, 105, 28461-28475.**https://doi.org/10.1029 /2000JB900326**.

Roberts, A.P., Heslop, D., Zhao, X., Pike, C.R., 2014. Understanding fine magnetic particle systems through use of first-order reversal curve diagrams. Reviews of Geophysics 52, 557–602. https://doi.org/10.1002/2014RG000462.

Roberts, A.P., Tauxe, L., Heslop, D., Zhao, X., Jiang, Z., 2018. A critical appraisal of the "Day" diagram. Journal of Geophysical Research: Solid Earth 123, 2618–2644. https://doi.org/10.1002/2017JB015247.

Salama, W., El Aref, M., Gaupp, R., 2015. Spectroscopic characterization of iron ores formed in different geological environments using FTIR, XPS, Mössbauer spectroscopy and thermoanalyses. Spectrochimica Acta Part A: Molecular and Biomolecular Spectroscopy 136, 1816–1826. https://doi.org/10.1016 /j.saa.2014.10.090.

Santos, H. G. dos., Jacomine, P. K. T., Anjos, L. H. C. dos., Oliveira, V. Á. de., Lumbreras, J. F., Coelho, M. R., Almeida, J. A. de., Araújo Filho, J. C. de., Lima, H. Narciso., Marques, F. A., Oliveira, J. B. de., Cunha, T. J. F., 2025. Sistema Brasileiro de Classificação de Solos-SiBCS, sixth ed., Embrapa, Brasília.

Schwaminger, S.P., et al., 2017. Oxidation of magnetite nanoparticles: impact on surface and crystal properties. CrystEngComm 19, 246–255. https://pubs.rsc.org/en/content/articlehtml/2017/ce/c6ce02421a.

Schwertmann, U., 1985. The Effect of Pedogenic Environments on Iron Oxide Minerals. Springer Press, Berlin, Germany.

Silva Filho, L. A., Ker, J. C., Fontes, M. P. F., Camêlo, D. D. L., Corrêa, M. M., Cavalcante, L. C. D., Guimarães, L. D. M., 2019. Mineralogical evolution of magnetic Rhodic Oxisols under different lithological influences in Brazil. Rev Bras Cienc Solo, 43, e0190065. https://doi.org/10.1590/18069657rbcs20190065.

Soil Survey Staff. 2022. Keys to Soil Taxonomy, Thirteenth ed. USDA Natural Resources Conservation Service, United States.

Souza, A. de., Oliveira Junior, J. F. de., 2026. Multifractal assessment of hydroclimatic variability in Midwest Brazil using the hydroclimatic balance index (HBI): a comparison with the standardized precipitation index (SPI). Theoretical and Applied Climatology, 157, 682. https://doi.org/10.1007/s00704-026-06467-6.

Spassov, S., Heller, F., Kretzschmar, R., Evans, M. E., Yue, L. P., Nourgaliev, D. K., 2003. Detrital and pedogenic magnetic mineral phases in the loess/palaeosol sequence at Lingtai (Central Chinese Loess Plateau). Physics of the Earth and Planetary Interiors, 140, 255-275. https://doi.org/10.1016/j.pepi.2003.09.003.

Stumm, W., Sulzberger, B., 1992. The cycling of iron in natural environments: considerations based on laboratory studies of heterogeneous redox processes. Geochimica et Cosmochimica Acta, 56, 3233-3257. https://doi.org/10.1016/0016-7037(92)90301-X.

Tardy, Y., 1997. Petrology of Laterites and Tropical Soils, A. A. Balkema Publishers, Rotterdam.

Taylor, R.M., Maher, B.A., Self, P.G., 1987. Magnetite in soils: I. The synthesis of single- domain and superparamagnetic magnetite. Clay Miner. 22, 411–422. https://doi.org/10.1180/claymin.1987.022.4.05.

Teixeira, P. C., Donagemma, G. K., Fontana, A., & Teixeira, W. G., 2017. Manual de métodos de análise de solo, third ed. Embrapa, Brasília.

Thompson, R., Oldfield, F., 1986. Environmental Magnetism. Springer, London. https:// doi.org/10.1007/978-94-011-8036-8.

Tite, M. S., Linington, R. E., 1975. Effect of climate on the magnetic susceptibility of soils. Nature, 256, 565-566. https://doi.org/10.1038/256565a0.

Torrent, J., Barrón, V., Liu, Q., 2006. Magnetic enhancement is linked to and precedes hematite formation in aerobic soil. Geophys. Res. Lett. 33, L02401. **https://doi.org/10.1029/2005GL024818**.

Torrent, J., Schwertmann, U., Fechter, H., Alferez, F., 1983. Quantitative relationships between soil color and hematite content. Soil science, 136, 6, 354-358.

Van Bemmelen, J., 1890. Ueber die Bestimmung des Wassers, des Humus, des Schwefels, der in den kolloidalen Silikaten gebundenen Kieselsäure, und des Mangans, im Ackerboden. Landwirtsch Versuchsstat, 37, e290.

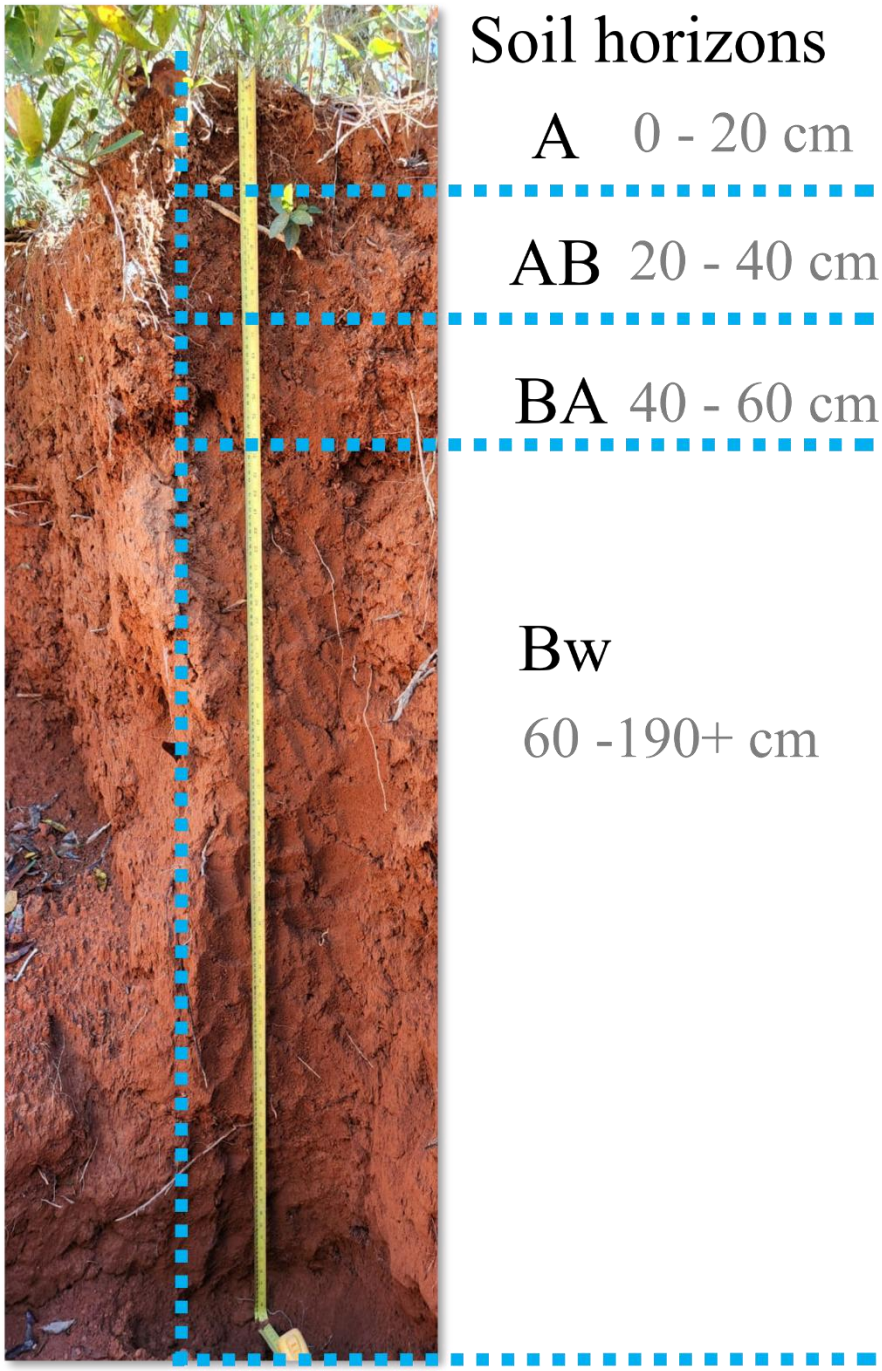
Verwey, E., 1939. Electronic conduction of magnetite (Fe3O4) and its transition point at low temperatures. Nature, 144, 327-328. https://doi.org/10.1038/144327b0.

Viana, J. H. M., Couceiro, P. R. D. C., Pereira, M. C., Fabris, J. D., Fernandes Filho, E. I., Schaefer, C. E. G. R., Rechenberg, H. R., Abrahão, W. A. P., Mantovani, E. C., 2006. Occurrence of magnetite in the sand fraction of an Oxisol in the Brazilian savanna ecosystem, developed from a magnetite-free lithology. Soil Research, 44, 71-83. https://doi.org/10.1071/SR05034.

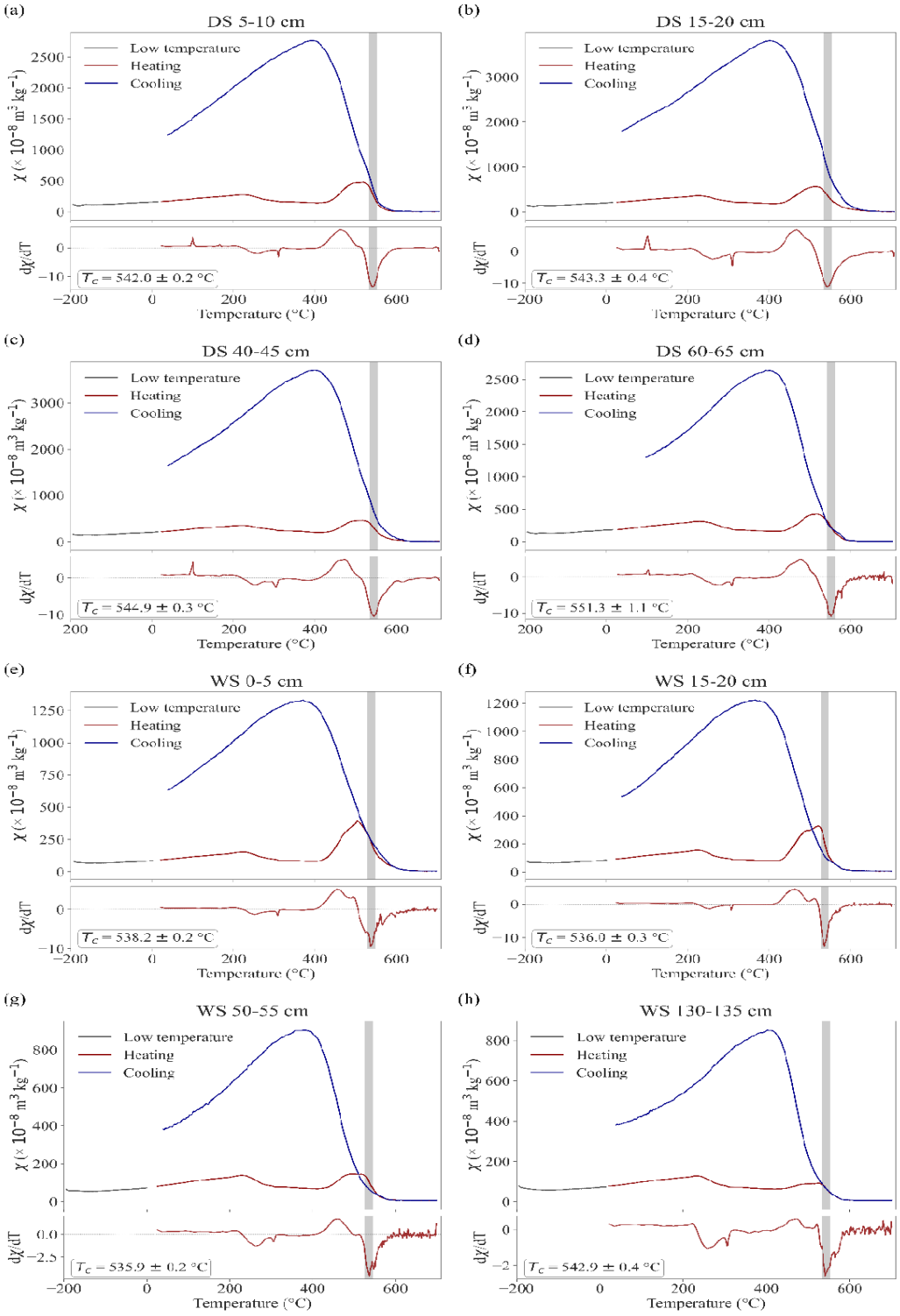
Zhang, D., Duan, Z., Chen, J., Wang, J., Muga, G., Yang, Y., Wang, Y., Liu, Z., Algeo, T. J., Hong, H., Zhou, L., and Yin, K., 2025. Characteristics and paleoclimate significance of authigenic ferrimagnetic minerals in the Xuancheng red earth, southern China. Sci Rep, 15, 3457. https://doi.org/10.1038/s41598-025-87020-9.

Zhang, Q., Appel, E., Hu, S., Pennington, R. S., Meyer, J., Neumann, U., Burchard, M., Allstädt, F., Wang, L., Koutsodendris, A., 2020. Nano-magnetite aggregates in red soil on low magnetic bedrock, their changes during source-sink transfer, and implications for paleoclimate studies. Journal of Geophysical Research: Solid Earth, 125, e2020JB020588. **https://doi.org/10.1029/2020JB020588**.

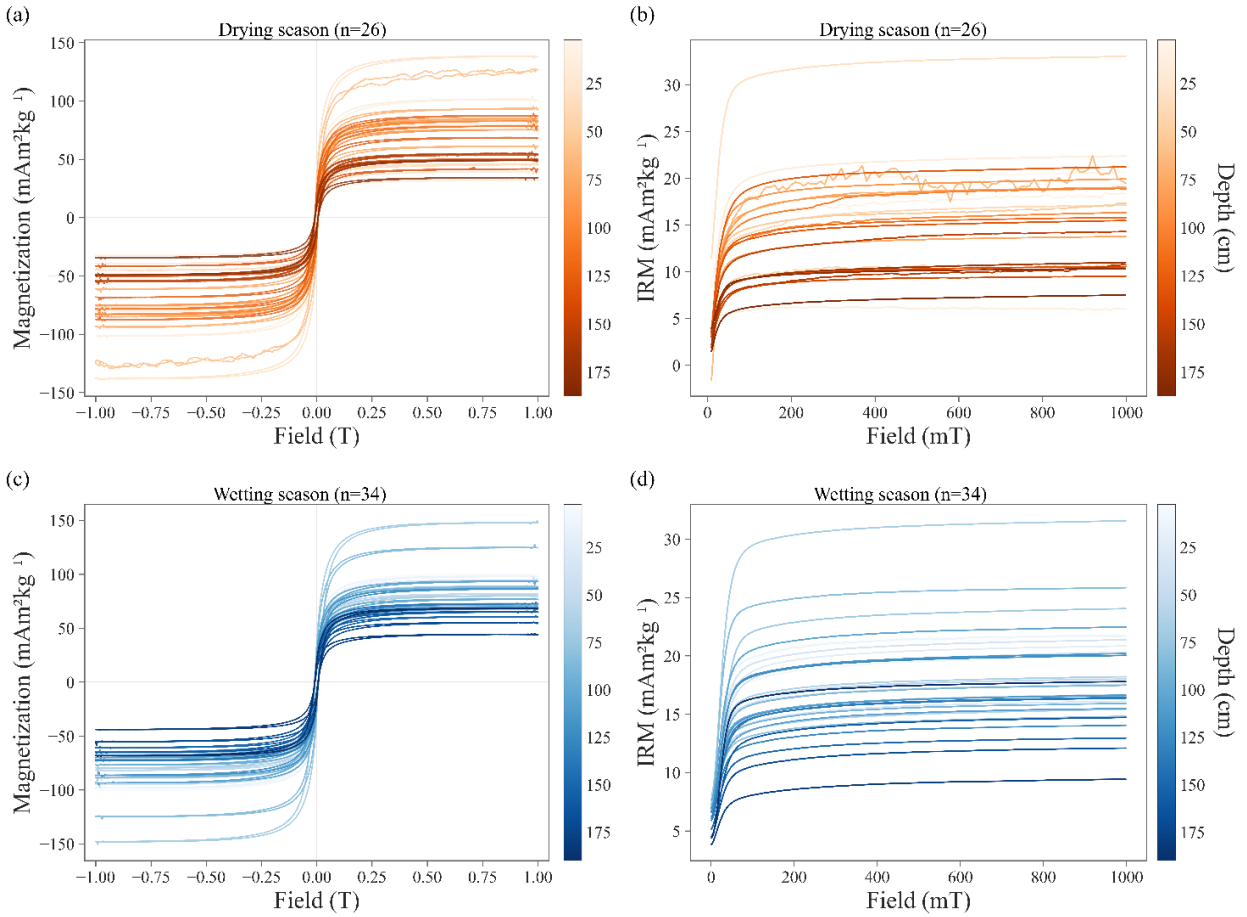
Supplementary figures



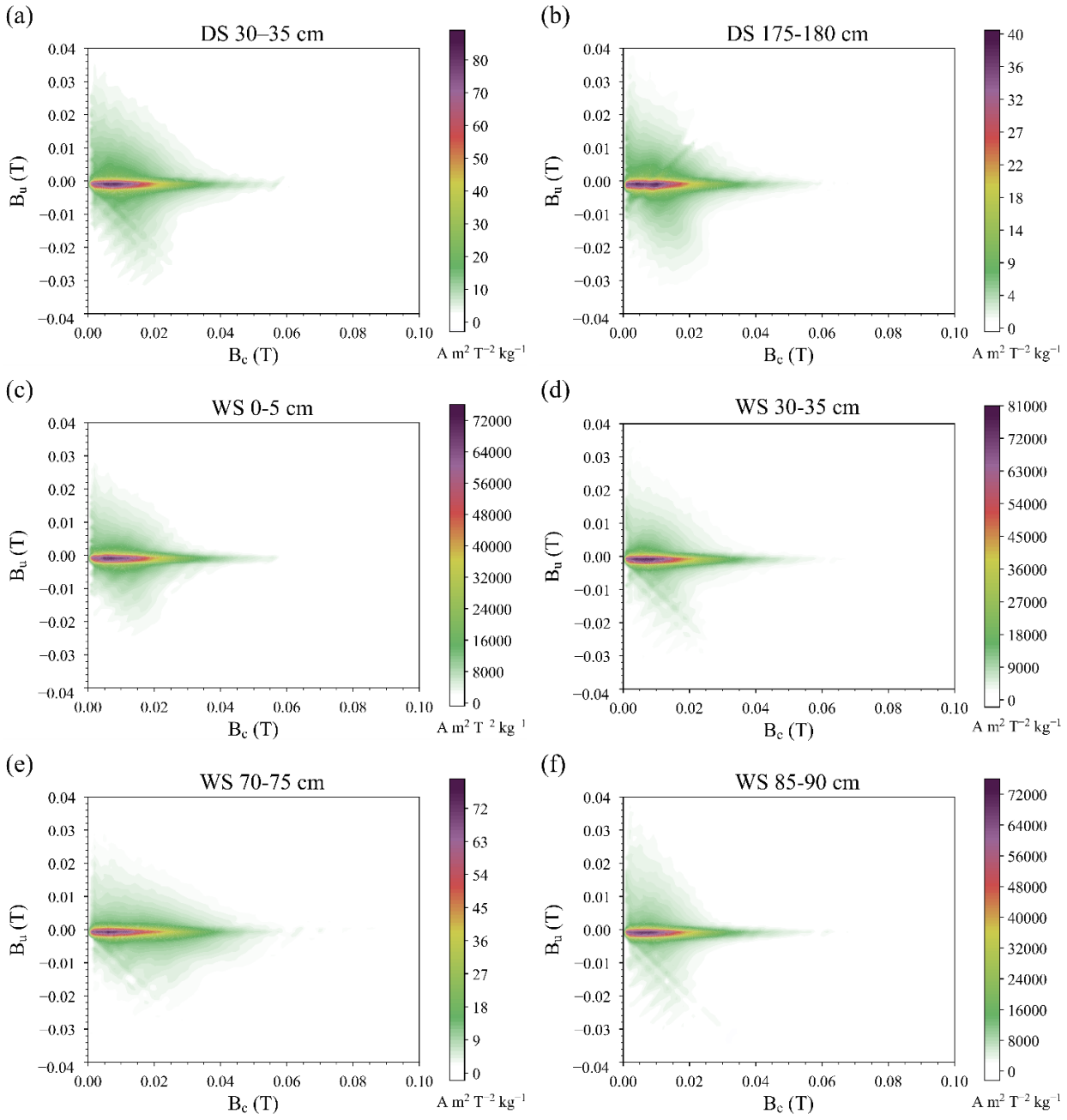
SFig. 1. Description of the *Latossolo Vermelho Ácrico Típico* (LVw) (Oxisol/Ferralsol) profile studied.



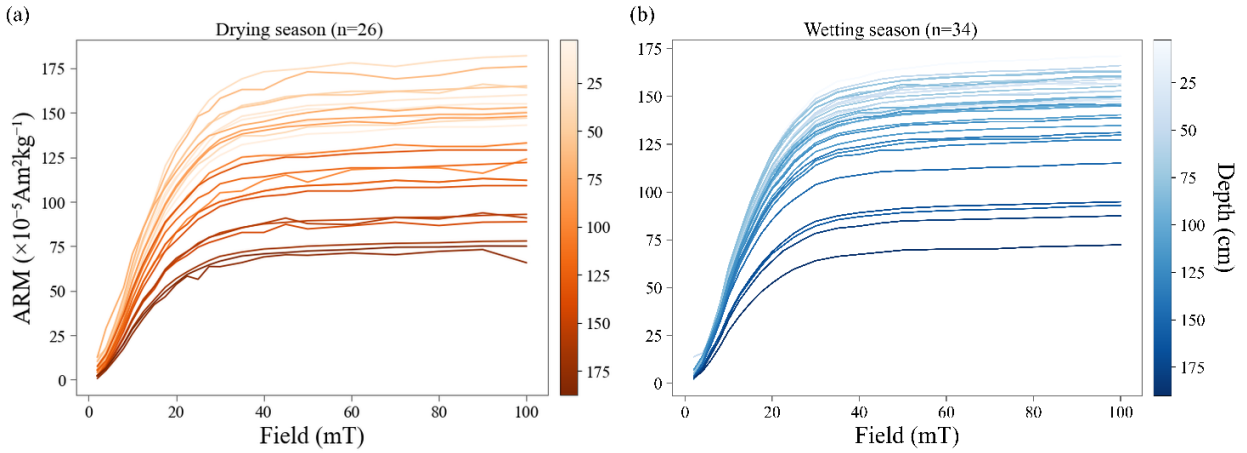
SFig. 2. Low- and high-temperature thermomagnetic curves measured at profile depth for the drying season samples (a–d) and wetting season samples (e–h).



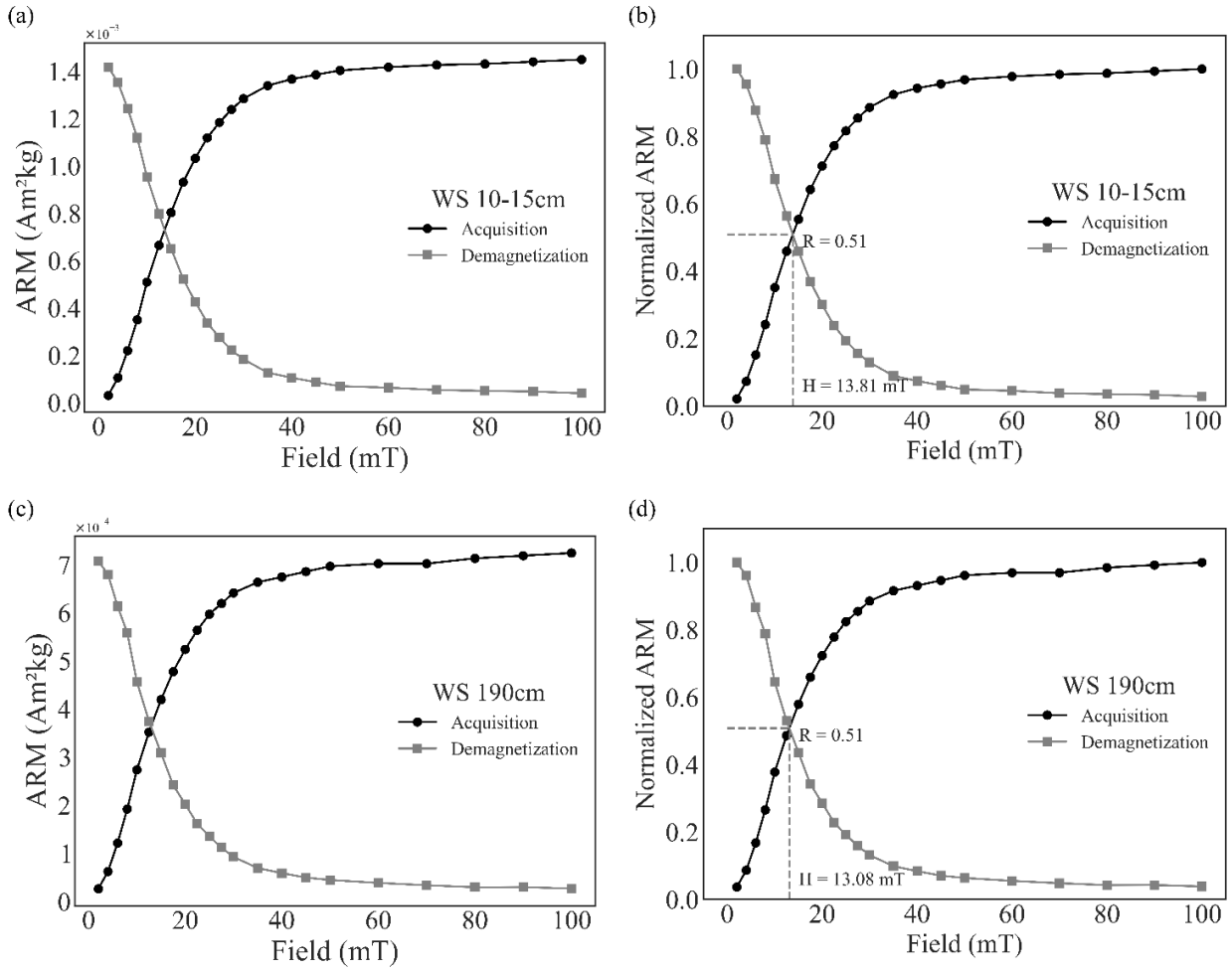
SFig. 3. Magnetic hysteresis loops (a, c) and Isothermal Remanent Magnetization (IRM) (b, d) for the drying and wetting season samples.



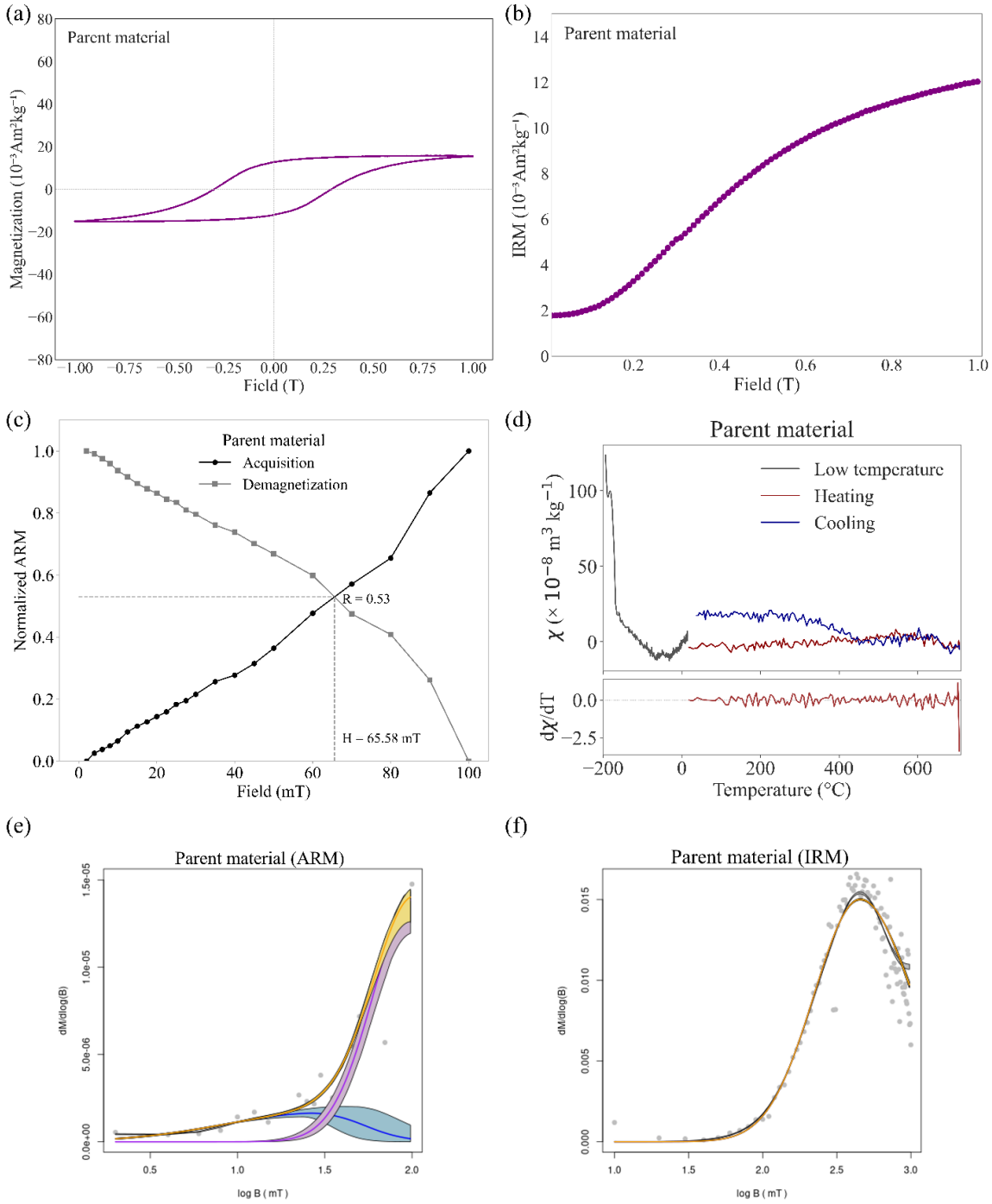
SFig. 4. First-order reversal curve (FORC) diagrams for drying season samples (a, b) and wetting season samples (c–f).



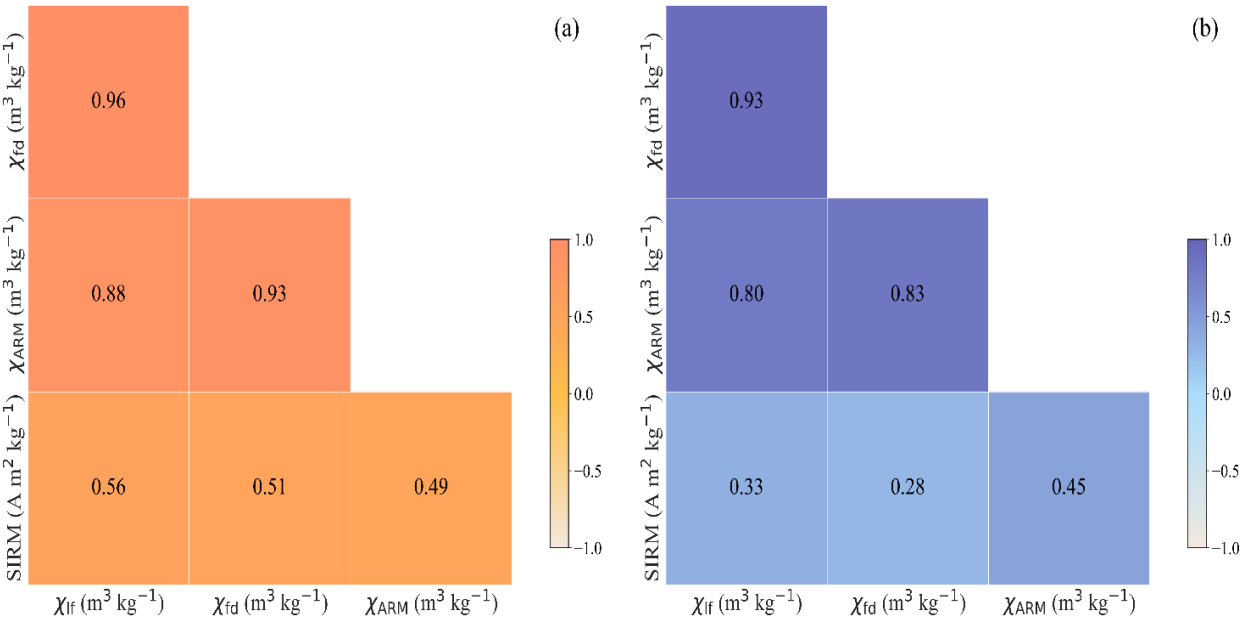
SFig. 5. Acquisition curves of Anhysteretic Remanent Magnetization (ARM) for drying season (a) and wetting season (b) samples.



SFig. 6. Examples of acquisition and demagnetization curves of Anhysteretic Remanent Magnetization (ARM) for wetting season samples (a, c), and Cisowski-like test (1981) (b, d).



SFig. 7. Magnetic properties of the parent material (slate): hysteresis loop (a), Isothermal Remanent Magnetization (IRM) (b), Cisowski-like test (c), low and high-temperature thermomagnetic curves (d), decomposition of ARM (e) and IRM (f) coercivity spectra using the MaxUnmix software (Maxbauer et al., 2016b).



SFig. 8. Spearman's rank correlation coefficients for drying season samples (a) and wetting season samples (b).

Supplementary table

Table S1. Description of the *Latossolo Vermelho Ácrico Típico* (LVw) (Oxisol/Ferralsol) soil profile morphology.

Depth (cm)	Soil horizons	Munsell color		Texture	Structure			Consistence		
		Dry	Wet		Type	Grade	Size	Dry	Moist	Wet
0-20	A	5YR 3/4	5YR 3/4	Clay	Angular to subangular block (40%), krotovina (1%) and granular (59%)	Strong	Fine to coarse	Slightly hard	Friable	Slightly sticky and slightly plastic
20-40	AB	2.5YR 4/6	2.5YR 3/6	Clay	Angular to subangular block (40%), krotovina (1%) and granular (59%)	Strong	Fine to coarse	Slightly hard	Friable	Slightly sticky and slightly plastic
40-60	BA	2.5YR 4/8	2.5YR 3/6	Clay	Angular to subangular block (30%), krotovina (2%) and granular (68%)	Strong	Fine to coarse	Soft	Friable	Slightly sticky and slightly plastic

60-190+	Bw	2.5YR 4/8	2.5YR 3/6	Clay	Angular to subangular block (20%) and granular (80%)	Strong	Fine to medium	Soft	Friable	Slightly sticky and slightly plastic

Table S1. (continued) Description of the LVw soil profile morphology.

Depth (cm)	Pores		Roots		Boundary	
	Quantity	Size	Quantity	Size	Topography	Distinctness
0-20	Many	Fine	Many	Fine to medium	Smooth	Gradual
20-40	Many	Fine	Common	Fine to medium	Smooth	Diffuse
40-60	Many	Fine	Few	Fine to medium	Smooth	Diffuse
60-190+	Many	Fine	Few	Fine to medium	-	-